Chapter-4

Influence of ionic radii on the conduction mechanism in Lanthanum silicate oxyapatite

Ashishkumar Yadav, Priyanka A. Jha , Pardeep K. Jha, Neetu Jha and Prabhakar Singh,

Materials Chemistry and Physics 297(2023)127444 DOI:
https://doi.org/10.1016/j.matchemphys.2023.127444

CHAPTER 4: Influence of ionic radii on the conduction mechanism in Lanthanum silicate oxyapatite

4.1 Introduction

Oxide ion conductors (OICs) have attracted researchers due to their significant role in electrochemical conversion devices (solid oxide fuel cell (SOFC)) [110]. SOFC is a technology helping to solve the current energy problems i.e., supply and demand by providing a solution to environmental pollution[111], [112] . Here the recent increase in demand has come from the domestic sector which requires low temperature fuel cells. For this, low temperature oxide ion conductors working in the temperature range (500 K - 800 K) will be helpful in designing low temperature electrochemical solid oxide fuel cells [113]. High temperature fast oxide ion conductors cannot work due to the sharp decrease in conductivity with temperature. Hence, oxide ion conductors in the low temperature and intermediate temperature are required.

Recently, apatite type rare earth silicates (discovered by Nakayama in 1995[114]) have attracted the researchers due to their low activation energy in the ionic conduction [115]. Thus, they prove their suitability to work in the intermediate temperature range. Various synthesis techniques have been employed from the c-axis orientation and porosity optimization and in turn, their effects on conductivity. The nano structuring of these compounds is still in infant stage and more work is required from the researchers. Moreover, porous network is obtained in these compounds with the formation of lanthanum nanodomains[116]. However, sol-gel technique is used to synthesize spherical nanoparticles [117] but their conductivity is not yet studied.[118]–[120]

Among these OICs, lanthanum silicate oxyapatite i.e., $La_{10-\alpha}^{3+}(SiO_4)_6^{4-}O_{2+\delta}^{2-}(LSO)$ is one of the most interesting materials due to its anisotropic ion conduction[121], [122]. Its hexagonal structure possesses an array of oxygen ions along c-axis, lanthanum ions surrounding the oxygen ions, SiO4 cluster and another lanthanum in between the clusters [123]–[126]. In the structure lanthanum vacancies are included in order to maintain charge neutrality and oxygen conduction along c- axis takes place [127], [128]. Further, it can be expected to be modify with the substitution. Thus, there is scope of conductivity enhancement in polycrystalline LSO with grain alignment (i.e. ($\sigma_c^{\parallel} / \sigma_c^{\perp} > 10$ i.e., conductivity in direction of grains parallel to c-axis is ten times larger than conductivity in direction of grains perpendicular to c-axis)) [121] and doping [129]. and doping. There are studies claiming that oxygen interstitial, Oi, is the dominant charge carrier for conduction rather than typical oxygen vacancies with a diffusion barrier of 0.5-0.8 eV [130], [131]. This barrier accounts for the contribution of lanthanum vacancy as well [132]. If lanthanum vacancy can be reduced then this barrier might reduce. Lanthanum vacancy are created by charge balance and their concentration is maintained by aliovalent elemental substitution [133] as in the case of perovskites[134], [135]. Various doping such as Al, Mg at B-site [136] and Alkaline earth [137]–[142] and rare earth substitutions at A-site [133] have been done in order to stabilize their structure and change the conduction mechanism viz. push-pull and interstitial are well described for the oxyapatites but its dynamics is still scarce. Further, substitution can bring some unusual thermodynamics and possibility of altered defect-formation is quite possible[143] . Thus, the effect of ionic radii on the structural and dynamics disorder in parent $\mathrm{La}_{10-\alpha}^{3+}(\mathrm{SiO}_4)_6^{4-}\mathrm{O}_{2+\delta}^{2-}$ and substituted $(\mathrm{La}_{1-x}\mathrm{A}_x)_{10-\alpha}(\mathrm{SiO}_4)_6\mathrm{O}_{2+\delta}$ (x

= 0.0, 0.05, 0.10 and 0.15) where A= Ca and Ba compounds is studied via structural, electrical, optical and thermal studies.

4.2 Composition section

The ionic conductivity depends on the product of occupancy of oxygen ion and its vacancy. Further, the creation of oxygen vacancies in case of apatites depends upon lanthanum content. For this, we define two parameters δ, (+ve value represents oxygen excess and -ve value represents oxygen deficiency) and α, lanthanum deficiency. La can be substituted with divalent metals, A. Further, the composition can be defined with the help of equation 4.1 written in Kroger Vink notation. It can be seen that CO and O_2 gas are evacuated with the formation of La and O vacancies

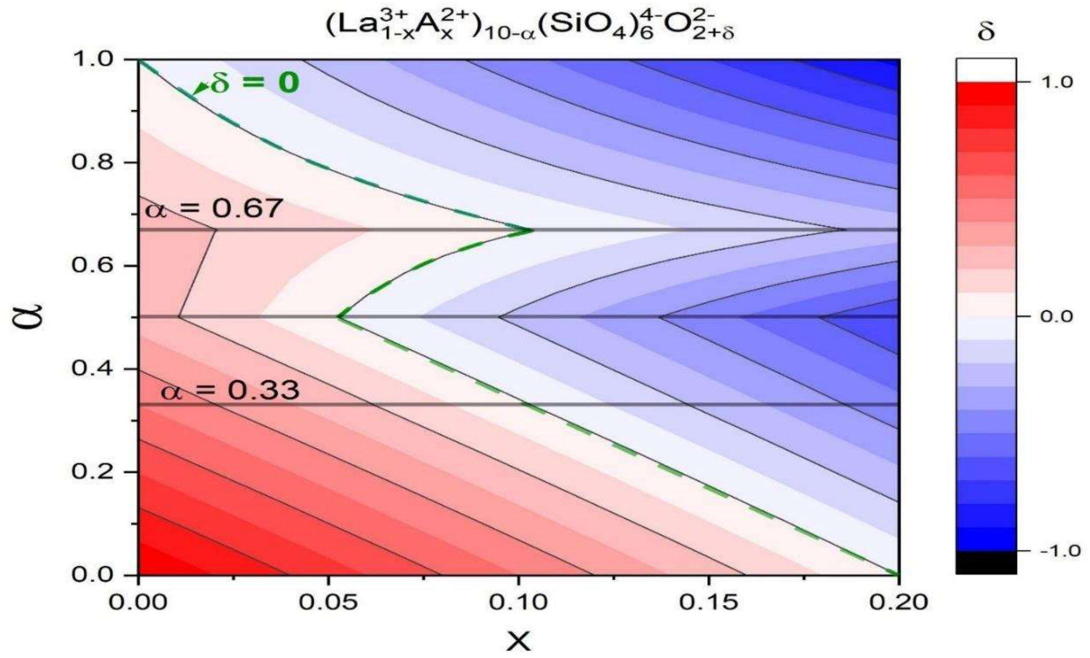

Figure 4.1. Variation of La content with O vacancies on varying x, for x > 0.1, oxygen vacancy formation is more as compared to oxygen vacancy formation for x < 0.1. However, at x = 0.1, La content and O vacancy are quite balanced

$$(5-x)La_2O_3 + xACO_3 + 6SiO_2 \rightarrow La_{(10-x-\alpha)}A_xSi_6O_{(26+\delta)} + xCO \uparrow + \left(x+\frac{1}{2}\right)O_2 \uparrow + \alpha V_{La}^{3+} + \delta V_O^{2-} \qquad (4.1)$$

It can be seen that CO and O_2 gas are evacuated with the formation of La and O vacancies. The interrelation between La vacancies (in terms of α) and O vacancies (in terms of δ) with aliovalent substitution at La-site (in term of x) are pictorially represented as Figure 4.1 by fixing some values of α and x in equation 1. It can be seen that when α =1, with the increase in x, δ is -ve. In this region, the probability of formation of secondary phase increases. When α =0, with the increase in x, δ decreases but will always be +ve. In this regime, sample will be more electronic. For α =0.5, the substitution limit reduces to x = 0.05. For α = 0.67 and 0.33, it can be seen that for x > 0.1, oxygen vacancy formation is more as compared to oxygen vacancy formation for x < 0.1. However, at x = 0.1, La content and O vacancy are quite balanced. That's why, these two are the major choice of α. Here, in the present work, α = 0.33 is chosen and varied x up to 0.15 at the steps of 0.05 on the basis of charge neutrality.

Till now the charge compensation is only considered while the role of ionic radii is ignored. However, the ionic radius of substituents is pivotal parameter as it alters the average area of critical triangle (saddle point) significantly and therefore ion mobility. Here 'A' can be Ba, Sr and Ca and their ionic radii vary in the order of Ca (134 pm) > Sr (144 pm) > Ba (161 pm) with 12 coordination number. Figure 4.2 depicts the higher ion mobility volume (V_{IM}) for Ca substituted samples than Sr and Ba substituted samples i.e., with the increase in ionic radii ($<R_{i,\,La}>$) from Ca to Ba, ion mobility decreases. Moreover, it is also observed that with the increase in x of Ca, $<R_{i,\,La}>$ decreases and with the increase in Ba content, $<R_{i,\,La}>$ increases (Fig.2 (inset)).

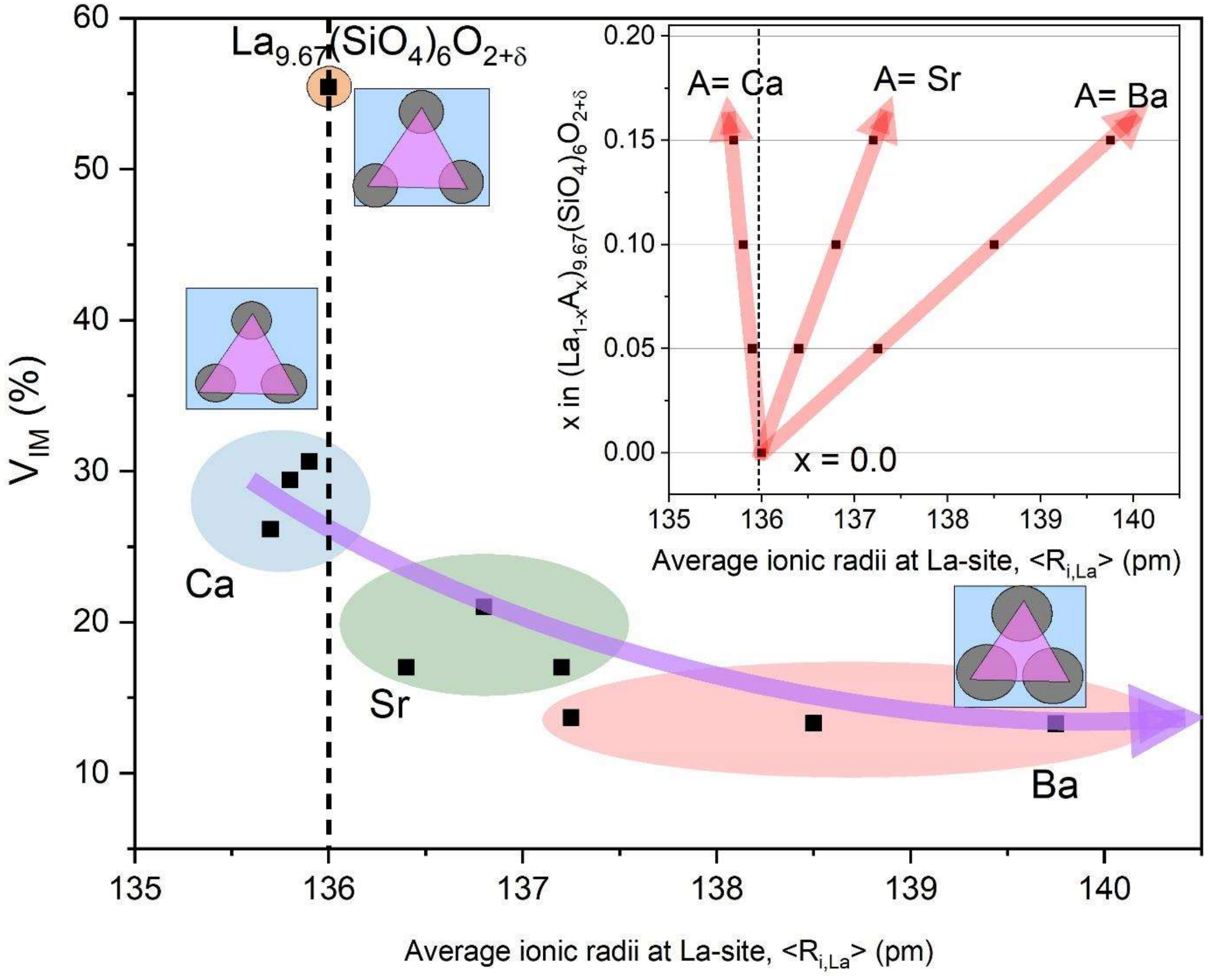

Figure 4.2: Variation of ion mobility volume with average ionic radii at La site as average ionic radii varies from Ca to Ba with the increase in their respective contents (inset) depicts the variation of ionic radii with the variation on Ba, Sr and Ca concentrations

4.3 MATERIALS AND METHODS

4.3.1 Sample preparations

Apatite based material $(La_{1-x}A_x)_{10-\alpha}(SiO_4)_6O_{2+\delta}$ $(x = 0.0, 0.05, 0.10\ and\ 0.15)$ with A = Ba and Ca were prepared using solid state route method. The constituent materials La_2O_3 (Sigma-Aldrich 99.9%), SiO_2 (Sigma-Aldrich 99.5 %), $CaCO_3$ (99%) and $BaCO_3$ (99%) were weighed stoichiometrically and thoroughly ground using mortar and pestle for

30-40 min. The obtained powder was then ground in ball-mill with propanol using zirconia ball and vial for 6 h maintaining the powder to ball weight ratio. The ball milled powder was calcined at 1000 ℃ for 8 h and phase determination of the calcined powder was done. Further, calcined powder was then ground and mixed with Polyvinyl alcohol (PVA) as a binder and pressed at 7 MPa to turn for palletization and pellets were then sintered at 1375 °C for 14 h at the heating rate of 5 $^{o}Cmin^{-1}$.

4.3.2 Characterization techniques

The phase identification of calcined powder and sintered pellets was done through Rigaku Miniflex powder diffractometer with Cu- Kα radiation (λ = 1.541 Å) and Ni filter in the range 2θ ~ 20 - 80 ° with a step size of 0.02 ° The XRD data was refined with P63/m symmetry using Full Prof Suite software package in structural Rietveld mode. After applying zero correction of the instrument, Pseudo - Voigt peak profile was used for refinement. The structure is studied using Diamond 3.0 software and bond distances along with lattice parameters are obtained. Further, bond valence sum (BVS) calculation is done using Full Prof software to find the percolation energy. The thermogravimetric analysis of the calcined powders was carried out simultaneous TG-DSC (Mettler Toledo, Germany) thermal analyzer in the temperature range 30$°C$ -1000 $°C$ at a constant heating rate of 10 $°C\ min^{-1}$ in the nitrogen atmospheres. The 3 h nearest neighbour hopping density of prepared sintered pellet was measured using density kit (Sartorius, BSA2245CW). The elemental compositions (EDAX) of the sintered pellets were characterized using scanning electron microscopy (EVO - Scanning Electron Microscope MA15 / 18). The average grain size was calculated using the linear intercept method. The electrical measurements was done using LCR meter (Wayne Kerr 6500P) in the temperature range 100 $°C$ to 700 $°C$ over the frequency range of between

20 Hz and 1 MHz. The elemental composition was further verified using X-ray photoelectron spectroscopy (Kratos Amicus model) high performance analytical instrument utilizing Mg target under 10^{-6} Pa pressure. The UV–VIS absorption spectra was taken by JASCO V-770 ultraviolet–visible (UV) spectrometer.

4.4 Results and Analysis

We have obtained single phase $(La_{1-x}A_x)_{10-\alpha}(SiO_4)_6O_{2+\delta}$ $(x = 0.0, 0.05, 0.10, 0.15)$ with $A = Ba\ and\ Ca$ compounds (Fig. 4.3 and Fig. 4.4 depicting X-ray diffractograms of all the samples with Rietveld refinement). The Table 4.1 and 4.2 shows the Wyckoff positions and occupancy for both the substitutes Ba and Ca.

4.4.1 Structural Studies

Figure 4.3 (left panel) shows the Rietveld refined X-ray diffractograms of Ba substituted samples where refinement is done with $P6_3/m$ symmetry using Full Prof Suite package with zero correction and Pseudo-Voigt peak profile. The goodness of fit ($\chi^2 < 10$) is also mentioned in Fig. 4.3(a). We have observed single phase lanthanum silicate and at x = 0.15, a secondary phase at $2\theta \approx 33^\circ$ corresponding to BaO is observed (JCPDS file No. 01-0746). Here, the peak splitting corresponding to $2\theta \approx 32^\circ$ doesn't completely disappear but reduces with the increase in x (Fig.4.3 right panel). Further, the peak is observed to be left shifted towards lower angle at x = 0.05, then it starts to shift to higher angle with the increase in x.

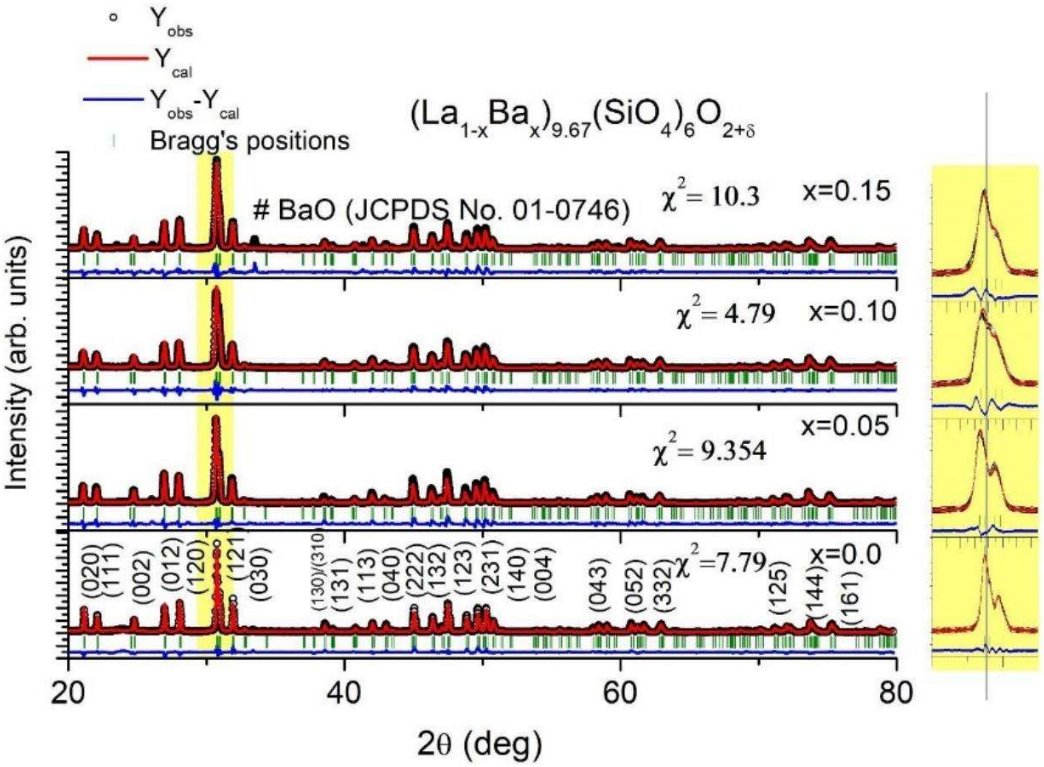

Figure.4.3 (a) Rietveld refinement of X-ray diffractograms of Ba substituted samples with $P6_3/m$ symmetry using Full Prof Suite package with Pseudo-Voigt peak profile. The goodness of fit ($\chi 2$) is lying within the appreciable range (Fig.4.2(a)). (b) splitting of the peak corresponding to $2\theta \approx 32^o$ reducing with the increase in x

The Rietveld refinement of X-ray diffractograms of Ca substituted samples done with $P6_{3/m}$ symmetry using Full Prof Suite package with Pseudo-Voigt peak profile is shown in Fig. 4.4(a)). The goodness of fit (χ^2) is lying within the appreciable range (Fig.4.3(a)). We have observed single phase lanthanum silicate and at x = 0.05, a secondary phase at $2\theta \approx 28^o$ corresponding to SiO_2 is observed (JCPDS file No. 89-1813). But this secondary phase diminishes at x = 0.1 and one more phase at $2\theta \approx 26^o$ appears at x = 0.15 sample corresponding to SiO_2 is observed (JCPDS file No. 89-1813). In addition, the splitting of the peak corresponding to $2\theta \approx 32^o$ disappears with the increase in x (Fig.4.4(b)). However, the peak is observed to be shifted towards a higher angle at x = 0.15 whereas there is nominal shifting at lower x content. The lattice parameter ‘c’ and La1-O4 bond length has shown a similar trend with x in Ba and Ca substituted samples (Fig.4.5 and 4.6 (a-b)).

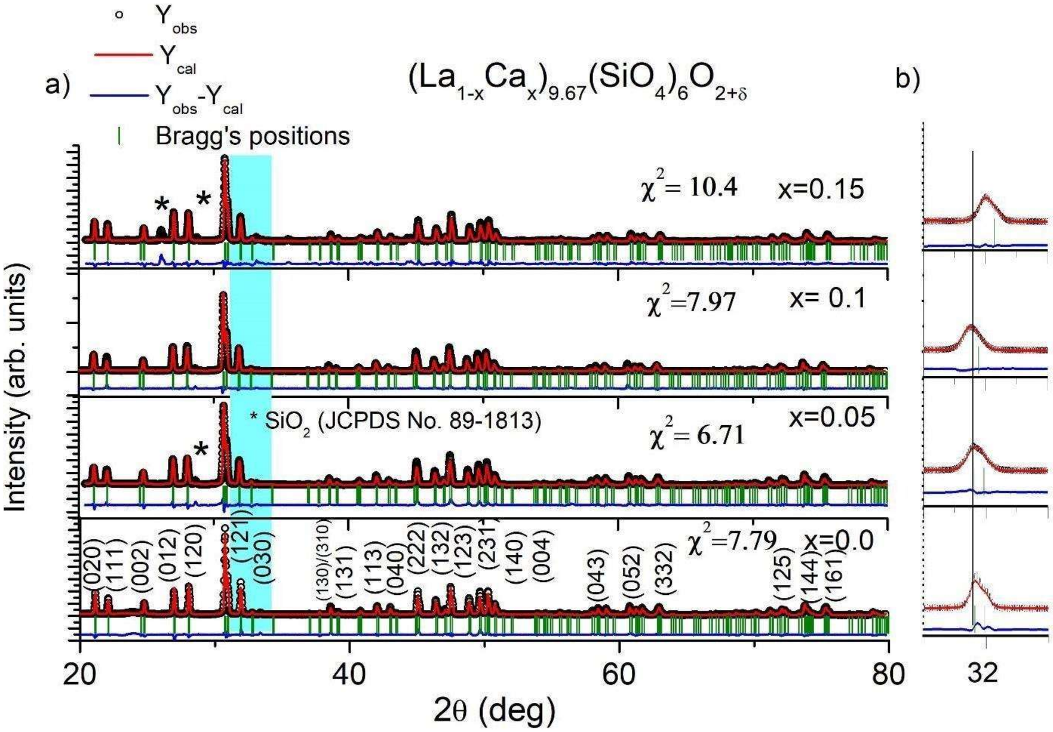

Figure.4.4 (a) Rietveld refinement of X-ray diffractograms of Ca substituted samples with P63/m symmetry using Full Prof Suite packagewith Pseudo-Voigt peak profile. The goodness of fit (χ2) is lying within the appreciable range (Fig.4.3(a)). (b) splitting of the peak corresponding to 2θ ≈ 32° disappearing with the increase in x

Further, the lattice parameters ‘a’ and ‘b’ have shown similar behaviour like La1(6h)-O4 bond length with x up to x = 0.10 in Ba substituted sample. Thus, for Ba substitution, the solid solubility limit exists up to x = 0.1 likewise Ca substitution. However, lattice parameter ‘b’ deviated at x = 0.15 due to BaO secondary phase formation. Further in Ca substituted sample, x = 0.15 showed exceptional behaviour due to secondary phase formation of SiO_2. The bond length maximum at x = 0.1

suggests the formation of big La-6h triangles that surround the O4 channel. Moreover, with the Ba substitution ion mobility volume has reduced three times in comparison to Ca substituted samples. Further, the samples synthesized are oxygen deficient instead of La deficient in Ca substituted samples. The occupancy obtained from Rietveld refinement is showing O deficient Ba substituted samples and La deficient Ca substituted samples (Table 4.1 and 4.2).

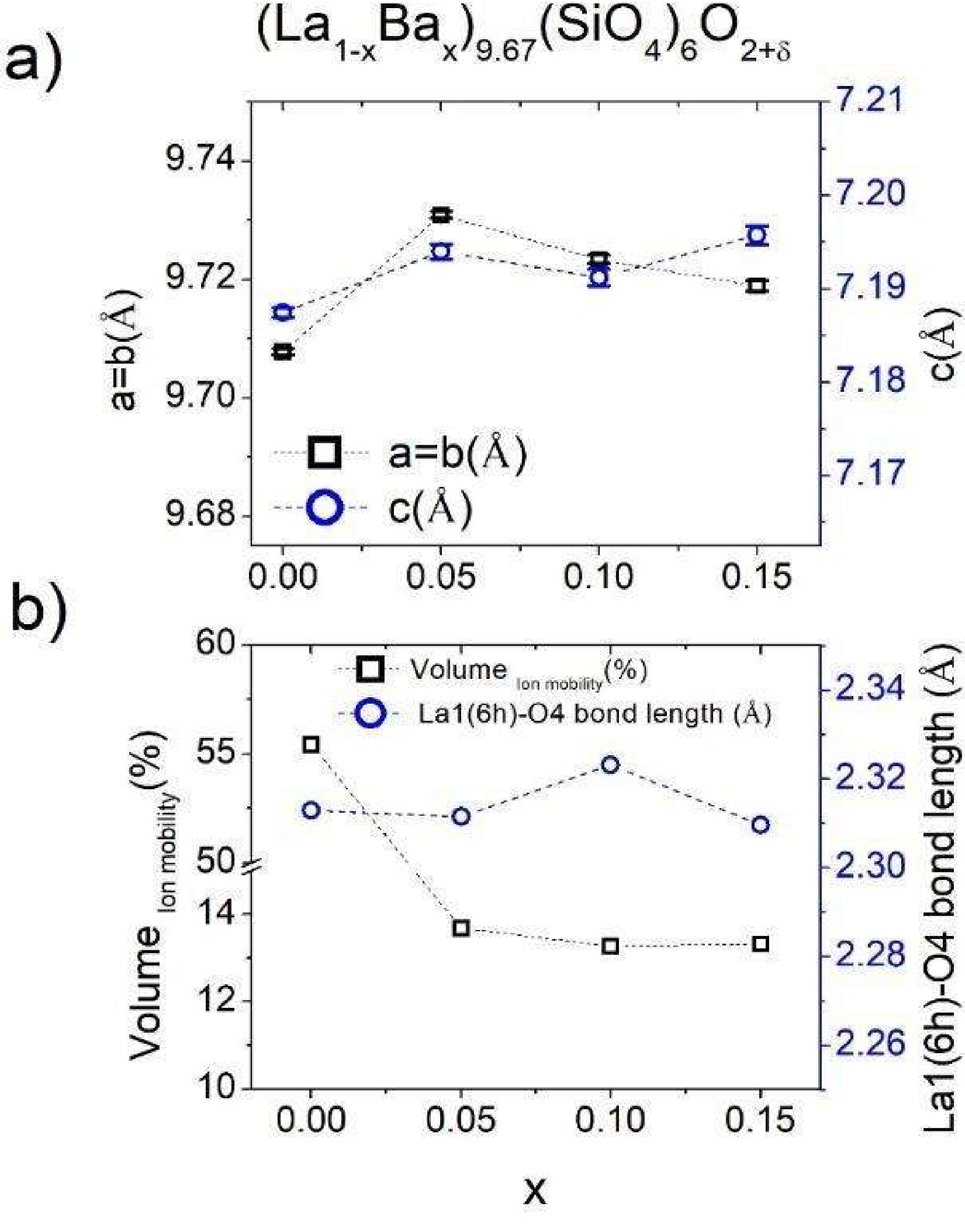

Figure 4.5 (a-b) Variation of Lattice parameters, La1(6h)-O4 bond distance of Ba modified $(La_{1-x}Ba_x)_{9.67}(SiO_4)_6O_{2+\delta}$ (x = 0.0, 0.05, 0.10 and 0.15)

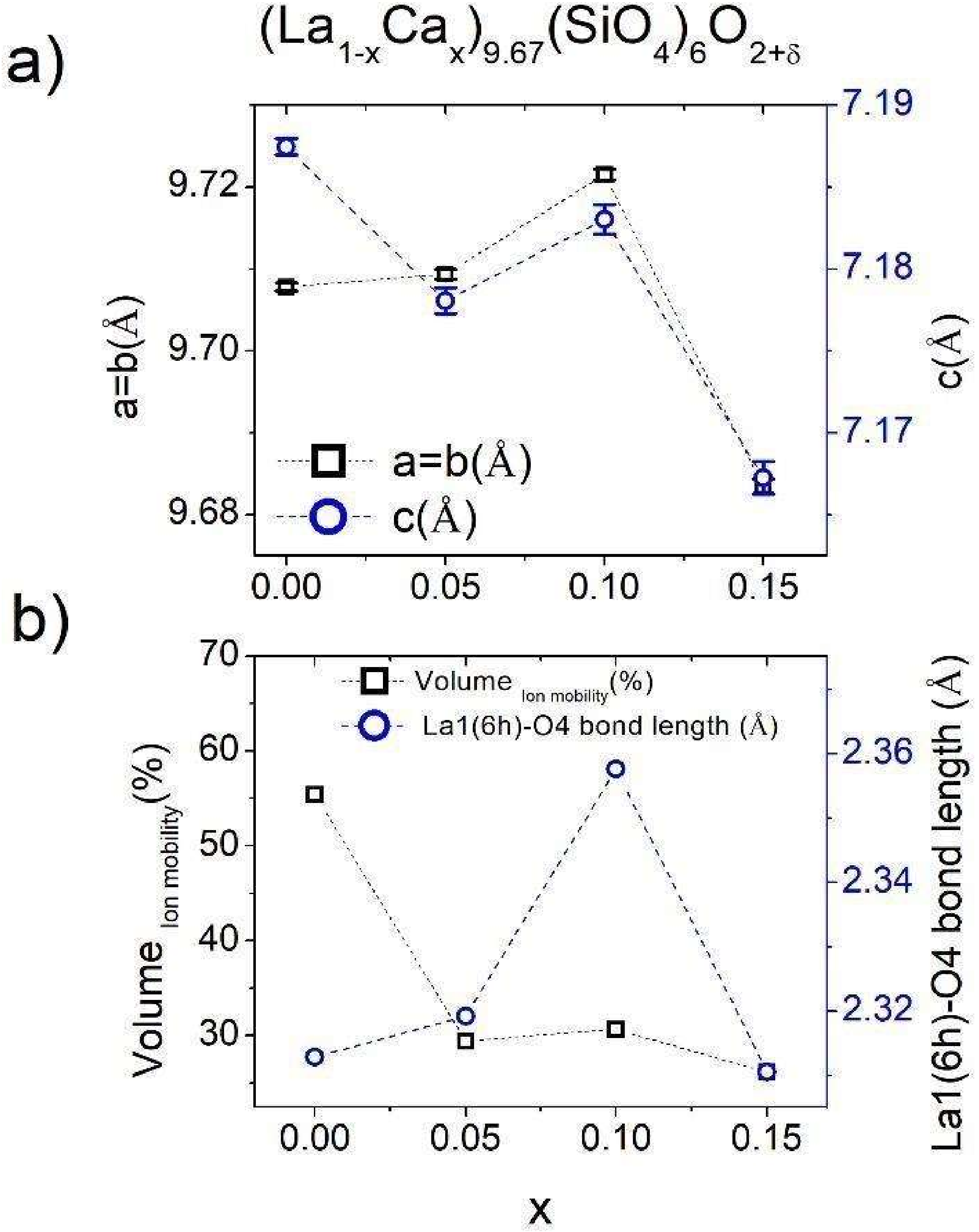

Figure 4.6 (a-b) Variation of Lattice parameters, La1(6h)-O4 bond distance of Ca modified $(La_{1-x}Ca_x)_{9.67}(SiO_4)_6O_{2+\delta}$ (x = 0.0, 0.05, 0.10 and 0.15)

Table 4.1 Wyckoff positions and occupancy obtained from refinement for Ba substituted samples

			Atomic Positions			
Composition	Atom	X	y	z	Occupancy	Stoichiometrically
x=0.0	La1	0.245	0.014	0.25	0.2	0.238
	La2	0.333	0.667	0.001		
	Si1	0.407	0.355	0.25	0.134	0.142
	O1	0.454	0.564	0.25	0.652	0.619
	O2	0.811	0.489	0.25		
	O3	0.257	0.325	0.062		
	O4	0	0	0.25		
x = 0.05	La1	0.243	0.011	0.25		
	La2	0.333	0.667	0.008	0.26	0.229
	Si1	0.407	0.375	0.25	0.153	0.142
	O1	0.418	0.534	0.25	0.578	0.619
	O2	0.843	0.514	0.25		
	O3	0.262	0.351	0.071		
	O4	0	0	0.25		
	Ba1	0.243	0.011	0.25		
	Ba2	0.333	0.667	0.009		
x = 0.10	La1	0.245	0.013	0.25	0.25	0.227
	La2	0.333	0.667	0.007		
	Si1	0.380	0.403	0.25	0.16	0.142
	O1	0.474	0.589	0.25	0.59	0.619
	O2	0.851	0.519	0.25		
	O3	0.257	0.346	0.067		
	O4	0	0	0.25		
	Ba1	0.245	0.013	0.25		
	Ba2	0.333	0.667	0.007		
x = 0.15	La1	0.244	0.014	0.25	0.24	0.226

	La2	0.333	0.667	0.006		
	Si1	0.376	0.407	0.25	0.162	0.142
	O1	0.467	0.604	0.25	0.59	0.619
	O2	0.843	0.507	0.25		
	O3	0.265	0.351	-0.063		
	O4	0	0	-0.25		
	Ba1	0.244	0.014	0.25		
	Ba2	0.333	0.667	0.006		

Table 4.2 Wyckoff positions and occupancy obtained from refinement for Ca substituted samples

Atomic positions						
Composition	Atom	X	y	Z	Occupancy	Stoichiometrically
x = 0.0	La1(6h)	0.245(3)	0.014(1)	0.25	0.212	0.238
	La2(4f)	0.333	0.667	0.001(2)		
	Si1	0.407(6)	0.355(5)	0.25	0.134	0.142
	O1	0.455(5)	0.565(2)	0.25	0.652	0.619
	O2	0.811(2)	0.489(9)	0.25		
	O3	0.257(8)	0.325(5)	0.0622(2)		
	O4	0	0	0.25		
x = 0.05	La1	0.244(7)	0.012(9)	0.25	0.083	0.229
	La2	0.333	0.667	0.008(7)		
	Si1	0.400(7)	0.378(4)	0.25	0.102	0.142
	O1	0.448(9)	0.565(1)	0.25	0.558	0.619
	O2	0.854(2)	0.535(8)	0.25		
	O3	0.251(4)	0.339(5)	0.071(2)		
	O4	0	0	0.25		
	Ca1	0.244(7)	0.012(9)	0.25	0.256	0.011
	Ca2	0.333	0.667	0.007(7)		
x = 0.10	La1	0.244(2)	0.011(2)	0.25	0.093	0.227
	La2	0.333	0.667	0.012(1)		
	Si1	0.399(3)	0.366(8)	0.25	0.091	0.142
	O1	0.4355(7)	0.556(8)	0.25	0.561	0.619
	O2	0.855(7)	0.52(2)	0.25		
	O3	0.252(2)	0.336(6)	0.074(8)		
	O4	0	0	0.25		

	Ca1	0.244(2)	0.011(2)	0.25	0.255	0.002
	Ca2	0.333	0.667	0.012(1)		
x = 0.15	La1	0.247(9)	0.009(5)	0.25	0.096	0.227
	La2	0.333	0.667	0.008(3)		
	Si1	0.423(5)	0.362(8)	0.25	0.094	0.142
	O1	0.414(9)	0.508(9)	0.25	0.551	0.619
	O2	0.835(3)	0.515(1)	0.25		
	O3	0.266(9)	0.351(1)	0.082(3)		
	O4	0	0	0.25		
	Ca1	0.247(9)	0.009(5)	0.25	0.257	0.003
	Ca2	0.333	0.667	0.008(3)		

4.4.2 SEM Analysis:

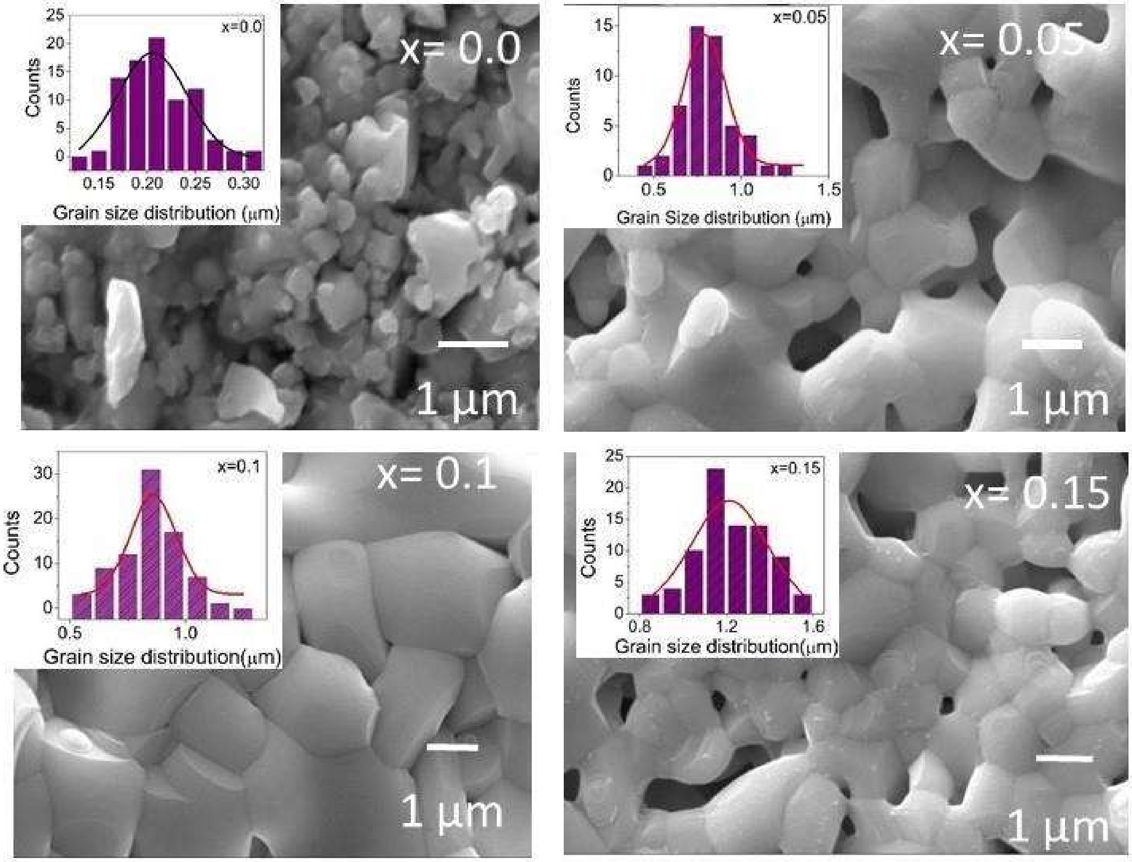

Figure 4.7 SEM micrographs and grain histograms of Ba modified $(La_{1-x}Ba_x)_{9.67}(SiO_4)_6O_{2+\delta}$ (x = 0.0, 0.05, 0.10 and 0.15)

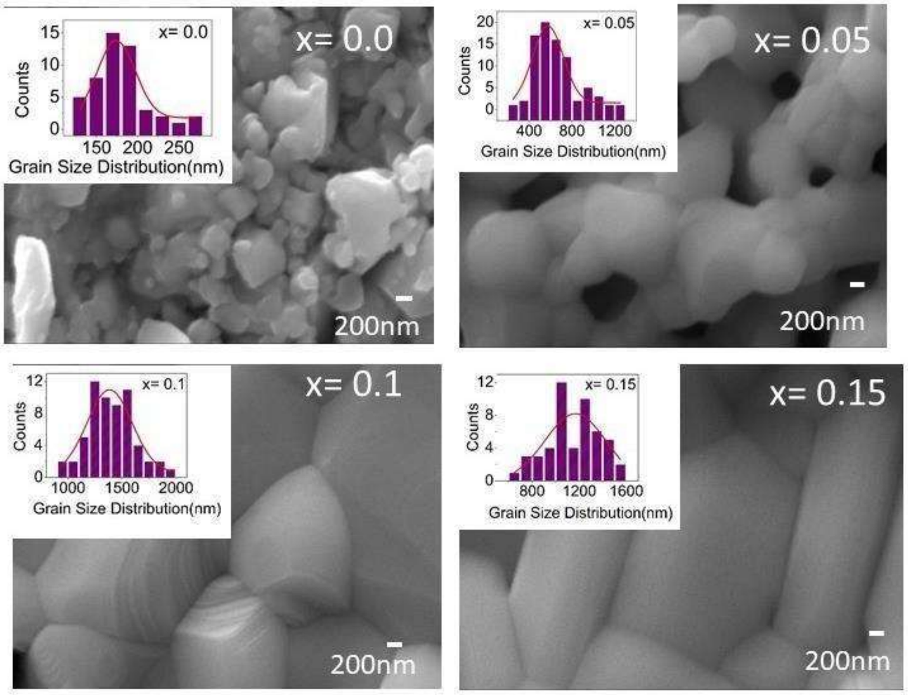

Figure 4.8 SEM micrographs and grain histograms of Ca modified $(\mathrm{La1\text{-}xCax})_{9.67}(\mathrm{SiO}_4)_6\mathrm{O}_{2+\delta}$ (x = 0.0, 0.05, 0.10 and 0.15)

The polycrystalline microstructure is observed for x = 0.0 and with the increase in x ($(\mathrm{La}_{1-x}\mathrm{Ba}_x)_{9.67}(\mathrm{SiO}_4)_6\mathrm{O}_{2+\delta}$ (x = 0.0, 0.05, 0.10 and 0.15)), the porosity reduces with the increase in grain size up to x = 0.1 (Fig.4.7). Further, hexagonal grains are observed for Ba modified samples. However, for x = 0.15, grains appear like stretched hexagons with some secondary phases. The average grain size has been estimated using grain size histograms and linear intercept method. The secondary phases visible in XRD are also visible in SEM micrographs of x= 0.15 sample. Further, grain morphology changes from porous to dense with the increase in x up to x = 0.1 and grain-boundary roughening is observed at x = 0.15. With the increase in O vacancies, rough grain boundaries have lower driving force for grain-boundary movement, leading to the increase in grain size.

The polycrystalline microstructure is observed for x = 0.0 and with the increase in x ($(La_{1-x}Ca_x)_{9.67}(SiO_4)_6O_{2+\delta}(x = 0.0, 0.05, 0.10\ and\ 0.15)$), the porosity reduces with the increase in grain size up to x = 0.1 (Fig.4.8). Further, hexagonal grains are observed up to x = 0.1. Exceptionally, for x = 0.15, grains are stretched and appear like stretched hexagons (rods). The secondary phases visible in XRD cannot be seen in SEM micrographs of x= 0.15 sample.

4.4.3 XPS and TGA Studies

To further analyse the secondary phase, elemental mapping suggests the inhomogeneous distribution of Si at grain and grain boundaries. Further, to determine the elemental concentration we have used XPS and TGA. Further, grain morphology changes from porous to dense with the increase in x up to x = 0.1 and changes from faceted to rough at x = 0.15. This change indicated grain- boundary roughening. With the increase in La content at x = 0.1, rough grain boundaries have lower driving force for grain-boundary movement, thus, leading to the increase in grain size. With the further increase in x and eruption of the secondary phase shown in Fig.4.8, the driving force elongated grains to perpendicular (XY) direction instead of XX direction. A gradual mass loss is observed in Thermogravimetric curves for Ba modified $(La_{1-x}Ca_x)_{9.67}(SiO_4)_6O_{2+\delta}$ (x = 0.0, 0.05, 0.10 and 0.15). In the parent sample, kinks correspond to the weight loss due to La and O_2. While with Ba substitution, these kinks correspond to the weight loss due to CO and O_2 as the weight loss observed in both the kinks are nearly 6% and 0.429% correspond to that of CO and O_2 (shown by orange and green arrows in Fig.4.9). Further, Rietveld refinement is also supporting the estimations done from XPS and TGA. While with

Ba substitution, these kinks correspond to the weight loss due to CO and O_2 as the weight loss observed in both the kinks are nearly 6% and 0.429% correspond to that of CO and O_2 (shown by orange and green arrows in Fig.4.9).

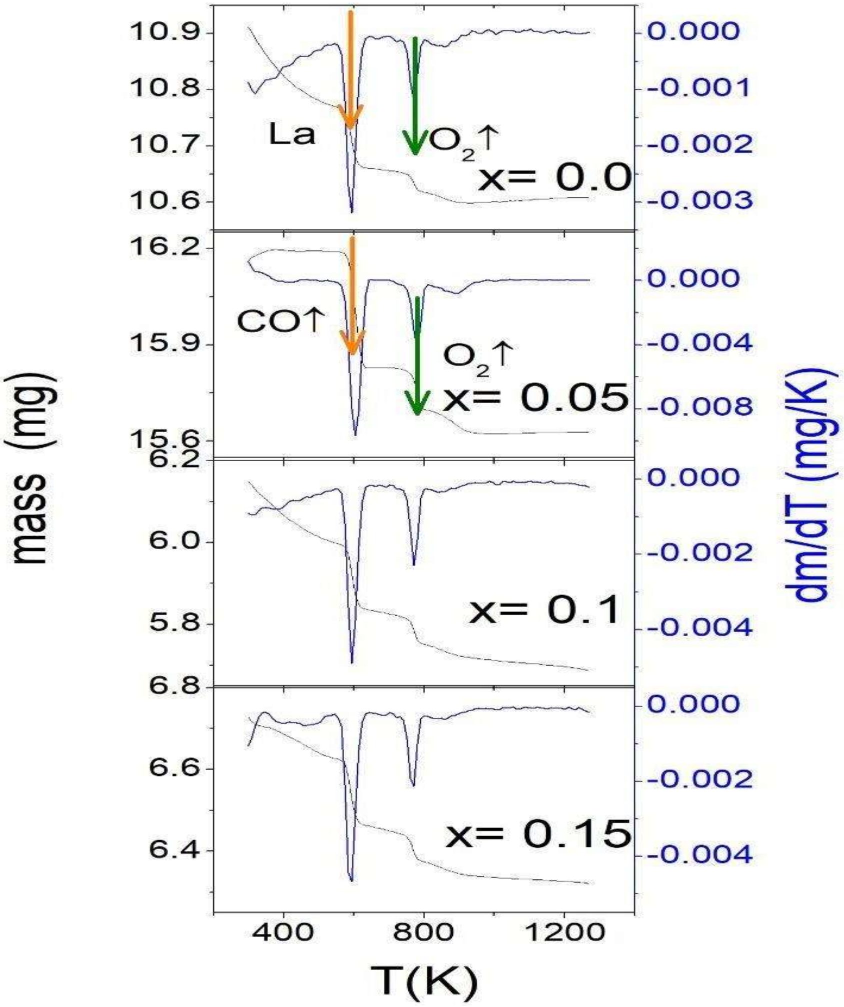

Figure 4.9 Thermogravimetric curves for Ba modified $(La_{1-x}Ba_x)_{9.67}(SiO_4)_6O_{2+\delta}$ (x = 0.0, 0.05, 0.10 and 0.15) showing the variation of mass loss and dm/dT with temperature

Further, Rietveld refinement is also supporting the estimations done from XPS and TGA.

$$5La_2O_3 + 6SiO_2 \rightarrow La_{10-\alpha}Si_6O_{26+\delta} + \alpha V_{La}^{3+} + \delta V_o^{2-}$$

$$(5-x)La_2O_3 + xBaCO_3 + 6SiO_2 \rightarrow La_{10-x-\alpha}Ba_xSi_6O_{26+\delta} + xCO\uparrow + \left(x+\frac{1}{2}\right)O_2$$

$$\uparrow + \alpha V_{La}^{3+} + \delta V_o^{2-}$$

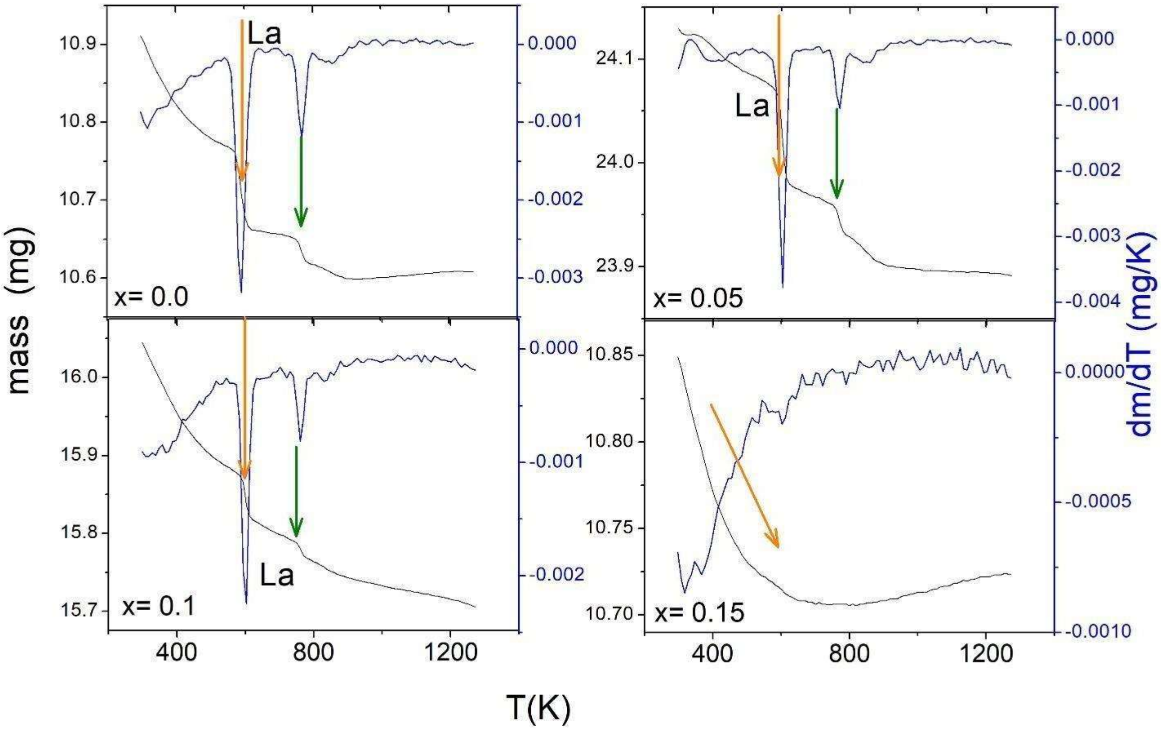

Figure 4.10 Thermogravimetric curves for Ca modified $(La1\text{-}xCax)_{9.67}(SiO_4)_6O_{2+\delta}$ (x = 0.0, 0.05, 0.10 and 0.15) showing the variation of mass loss and dm/dT with temperature

A gradual mass loss is observed in Thermogravimetric curves for Ca modified $(La_{1-x}Ca_x)_{9.67}(SiO_4)_6O_{2+\delta}$ (x = 0.0, 0.05, 0.10 and 0.15). Further, up to x = 0.10, two kinks are observedat ~500 K and 800 K (shown by orange and green arrows in Fig.4.10). These kinks correspond to the weight loss due to La as the weight loss observed in both the kinks is ~ 5.8%. The La deficiency observed is in accordance with the La content estimated from Rietveld refinement.

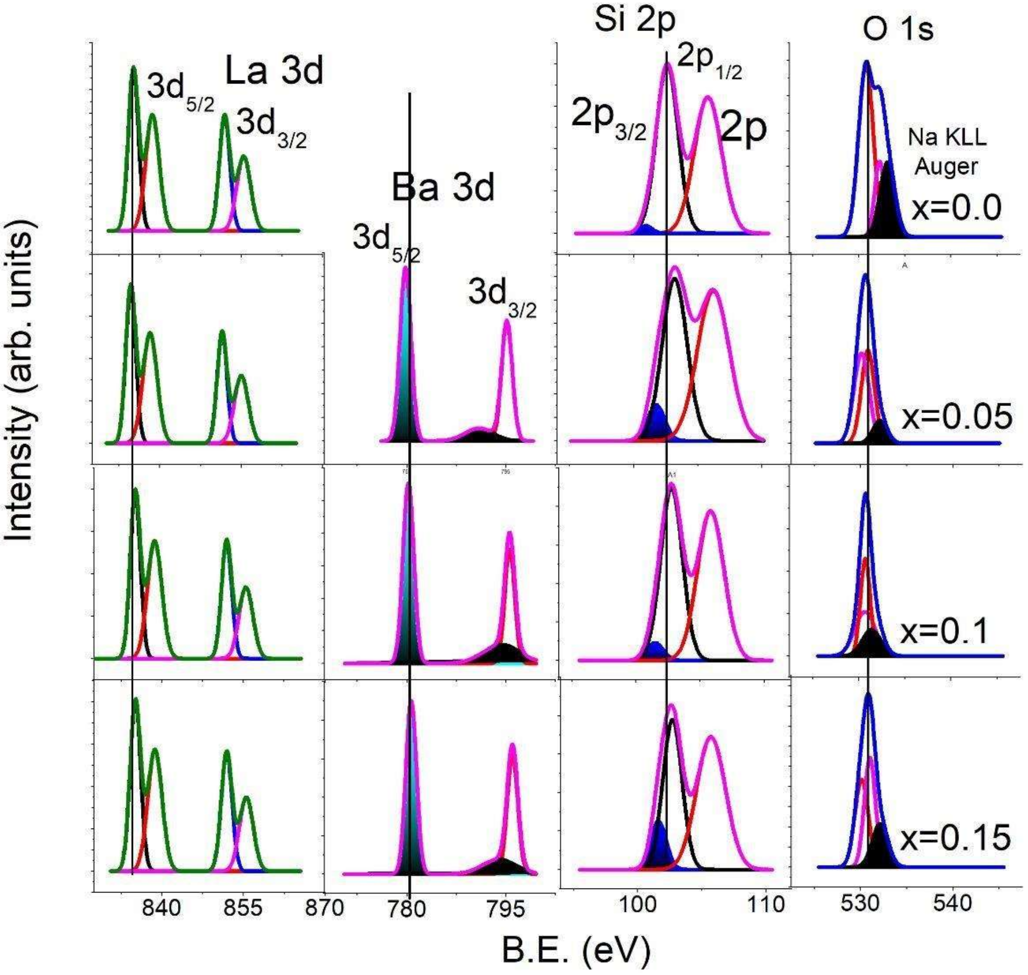

Figure 4.11 Deconvoluted X-ray photoelectron spectroscopy measurements of Ba modified $(La_{1-x}Ba_x)_{9.67}(SiO_4)_6O_{2+\delta}$ (x = 0.0, 0.05, 0.10 and 0.15)

X-ray photoelectron spectroscopy measurements of the $(La_{1-x}Ba_x)_{9.67}(SiO_4)_6O_{2+\delta}$ (x = 0.0, 0.05, 0.10 and 0.15) (Fig.4.11) are indexed with the standard look up table. Here, we have observed a peak shifting with x for $La3d_{5/2}$ component in Ba substituted samples while no peak shifting was observed for $La3d_{5/2}$ component in Ca substituted samples (Fig.4.12). In Ba3d spectra, chemical shift with the increase in x is observed along with Ba loss peak which is seen to be shifted with x and merging in Ba3d$_{3/2}$ peak. In the Si 2p spectrum Si 2p$_{3/2}$ intensity reduces at x = 0.1 and further increases for x = 0.15. Due to close spin-orbit splitting, we have observed asymmetric peaks corresponding to Si 2p. However, chemical shift of the spin orbit component is also observed. In O spectra, O 1s peak at ~ 529 eV is linked to the metal and O bond (La-O, Si-O and Ca-O) while, 2nd peak of O belongs to metal-OH bond. Oxygen vacancy concentration is linked to the ratio of peak area corresponding to the M-O and M-OH bond. Here, oxygen vacancy is observed to increase with x. Thus, oxygen content is decreasing and vacancy is increasing with the increase in x. Further, Na KLL Auger peak is observed in x = 0.0 and with the increase in x, Auger peak intensity reduces up to x = 0.1. Further, for x = 0.15, Auger peak intensity increases. Here, Ba substituted samples are more oxygen deficient and O deficiency is playing a critical role.

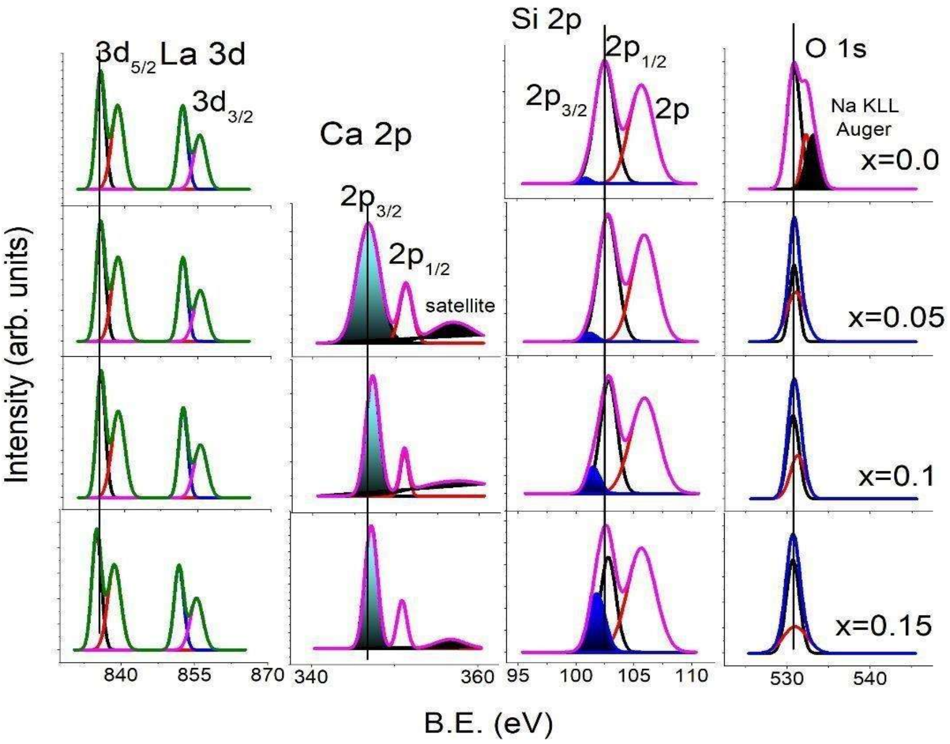

Figure 4.12: Deconvoluted X-ray photoelectron spectroscopy measurements of Ca modified $(La_{1-x}Ca_x)_{9.67}(SiO_4)_6O_{2+\delta}$ (x = 0.0, 0.05, 0.10 and 0.15)

Deconvoluted XPS data of the $(La_{1-x}Ba_x)_{9.67}(SiO_4)_6O_{2+\delta}$ (x = 0.0, 0.05,0.10 and 0.15) are shown in Fig.4.11. Further, no peak shifting is observed for La3$d_{5/2}$ component in Ca substituted sample. The intensity of Si 2p3/2 content is observed to increase with the increase in x showing the formation of secondary phase. However, chemical shift of the spin orbit component is also observed. In O spectra, O 1s peak at ~ 529 eV is linked to the metal and O bond (La-O, Si- O and Ca-O) while, 2nd peak of O belongs to metal-OH bond. Oxygen vacancy concentration is linked to the ratio of peak area corresponding to the M-O and M-OH bond. Here, the ratio of area of peaks is observed to decrease with the increase in x and showing the decrease in oxygen vacancy concentration with x. Thus, oxygen content is observed to increase and vacancy is observed to decrease with the increase in x. Further, Na KLL Auger peak is observed in x = 0.0 and with the increase in x, Auger peak diminishes. Simultaneously, intensity of satellite peak in Ca 2p spectra is increasing with x due to metal ligand interaction i.e. interaction of s- orbital of Ca and p-orbital of O (s-p interaction). In addition, the formation of $La(OH)_3$ suggests the formation of La vacancies and the samples are found to be La and Si deficient from the occupancies observed from the Rietveld refinement.

Table 4.3 δ obtained from TGA and XPS in Ca substituted sample

Composition	α obtained from TGA_N_2 atm	La obtained from XPS
x = 0.0	0.019	0.014
x = 0.05	0.013	0.150
x = 0.1	0.008	0.221
x = 0.15	0.014	0.152

Table 4.4 δ obtained from TGA and XPS in Ba substituted sample

Composition	δ obtained from TGA_N_2 atm	α obtained from TGA
x = 0.0	0.019	0.014
x = 0.05	-0.383	0.044
x = 0.1	-0.276	0.032
x = 0.15	-0.471	0.054

4.4.4 Temperature dependence conduction behaviour

4.4.4.1 dc conductivity

Figure 4.13 depicts $\sigma_{dc} - T$ plot for Ba and Ca substituted samples and in Ba substituted samples, conductivity increases upto x = 0.05 with x there after it decreases for x ≥ 0.1. However, for Ca substituted samples, conductivity increases upto x = 0.1 with x there after it decreases for x = 0.15. Further, $\sigma_{dc} - T$ curves are fitted with nearest neighbour hopping (NNH) model $\sigma T = \sigma_0 \exp\,(-\frac{E_a}{k_B T})$(individual colour lines). For T > 750 K fitting lines match well with the data but for T < 750 K fitted lines don't match well with the data. Further, the conductivity is observed to be higher for x = 0.1 in Ca substituted samples in comparison to the Ba substituted samples.

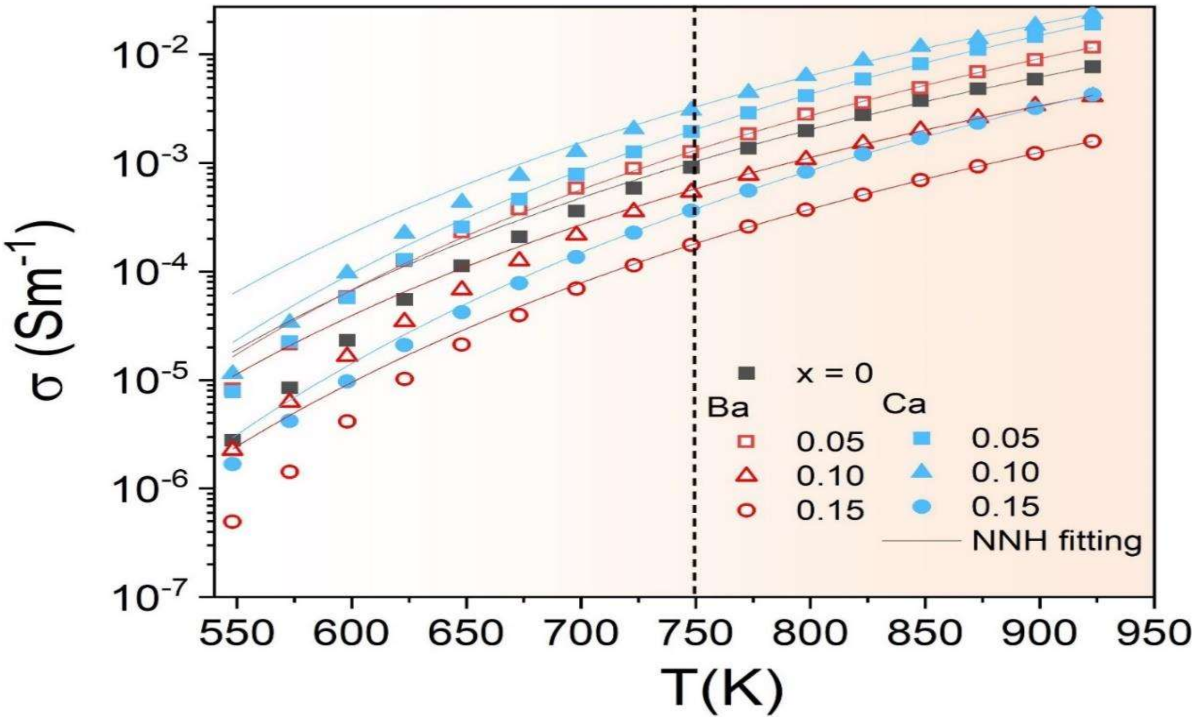

Figure 4.13. σ_{dc}_T plot for Ba and Ca substituted samples with nearest neighbour hopping

The deviation of fitted lines from the data points suggested to fit the data points in the two regimes. Further, Apatite structure doesn't show any kind of phase transition, but we have observed two slopes. Fig.4.14 depicts the Arrhenius plots in the two regimes and activation energies are estimated in the two regimes for all the samples. Most importantly, we have observed two slopes in the parent as well as substituted samples. At T < 700 K, a few ions get ionized leading to energy $E_{ion}/2$. The conductivity lowers for T< 700 K due to the slow movement of charge carriers. Moreover, for T > 700 K, more ions get ionized and thermally activated charge carriers participate in conduction.

The activation energies estimated in the two regimes are illustrated here (Fig.4.15(a)). We have observed E_a in the range of 0.9-1.1eV for T < 700 K. Further, for T > 700 K, E_a lies in the range of 0.7- 0.85 eV. This is in further correlation with the DFT studies suggesting the formation of oxygen vacancies and moving to interstitial sites. Fig. 4.15(b) shows the structure for the movement of interstitial oxygen vacancies, La1 and La2 form concentric hexagons in a-b plane with O4 in center and further O4 forms a channel along c-axis as shown in Fig. 4.15(c). Further, if any Frenkel defect would have been created with oxygen vacancy then activation energy would have risen to 4 eV [144]. Thus, in the present case, activation energy suggests thermally activated conduction via oxygen vacancies. Further, activation energy is not changing significantly with the ionic radii. Now, coming to the main observation why we observed the better conductivity for Ca (x= 0.1) than Ba (x = 0.1) which is contradictory to the literature [140]. Thus, hereafter, we will study the comparative of the two compositions with x = 0.1.

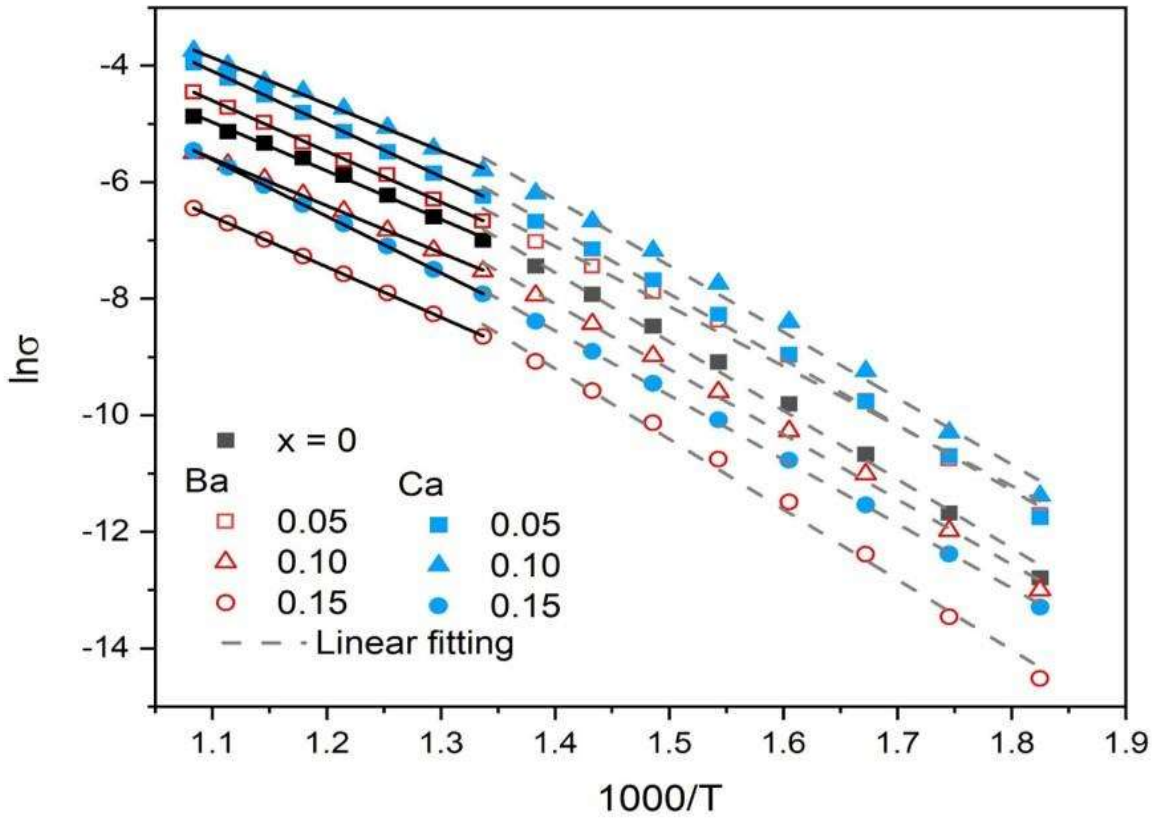

Figure 4.14 Arrhenius plots for Ca ad Ba substituted $(La_{1-x}A_x)_{10-\alpha}(SiO_4)_6O_{2+\delta}(x = 0.0, 0.05, 0.10\ and\ 0.15)$

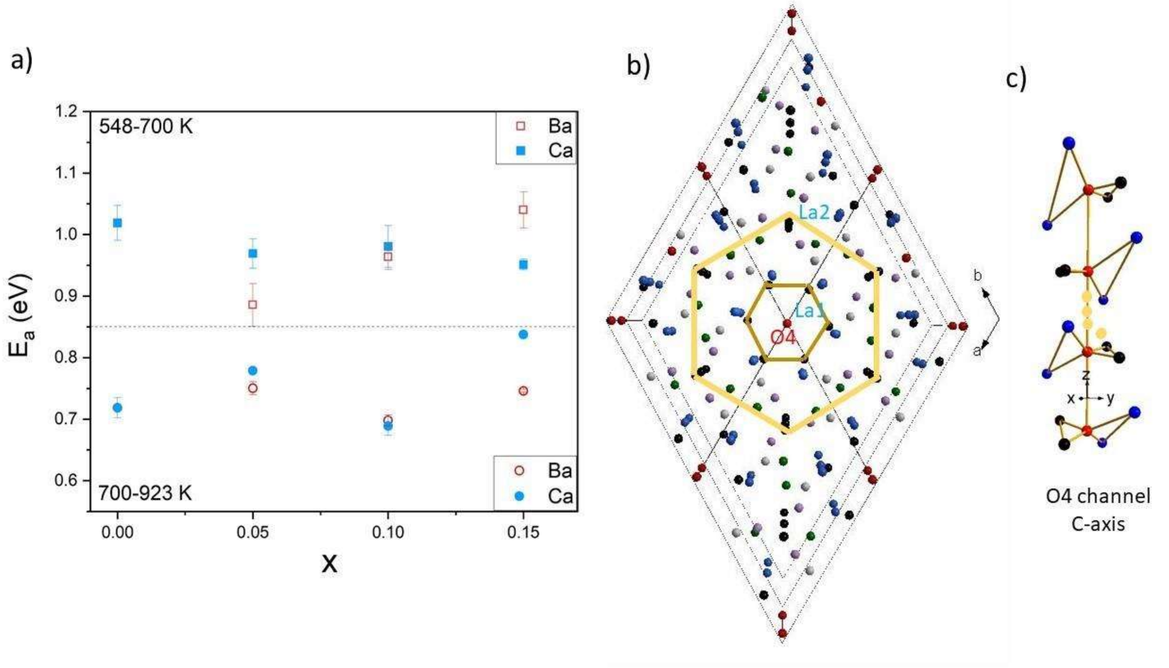

Figure 4.15 a) Activation energies for Ca ad Ba substituted $(La_{1-x}A_x)10-\alpha(SiO_4)_6O_{2+\delta}$ (x = 0.0, 0.05, 0.10 and 0.15) and b) shows the structure for the movement of interstitial oxygen vacancies, La1 and La2 form concentric hexagons in a-b plane with O4 in center and further O4 forms a channel along c-axis as shown in (c)

It can be seen from BVS calculation that with the Ba substitution ion mobility volume has reduced three times in comparison to Ca substituted samples (Fig.4.4, 4.5 and Fig.4.6). Further, the conductivity is higher for Ca substituted sample with x = 0.1. Figure 4.16 shows the variation of conductivity at 973 K with ion mobility volume and found that in Ba substituted samples, the conductivity reduces for x = 0.10 and x = 0.15 irrespective of the change of ion mobility volume. Further, in Ca substituted samples, the conductivity is higher for x = 0.1 but the ion mobility volume has varied with composition in the range of 27% to 29%. Inset shows the variation of conductivity with x. Now, the question arises, about the interplay of ionic radii with x and thus conductivity.

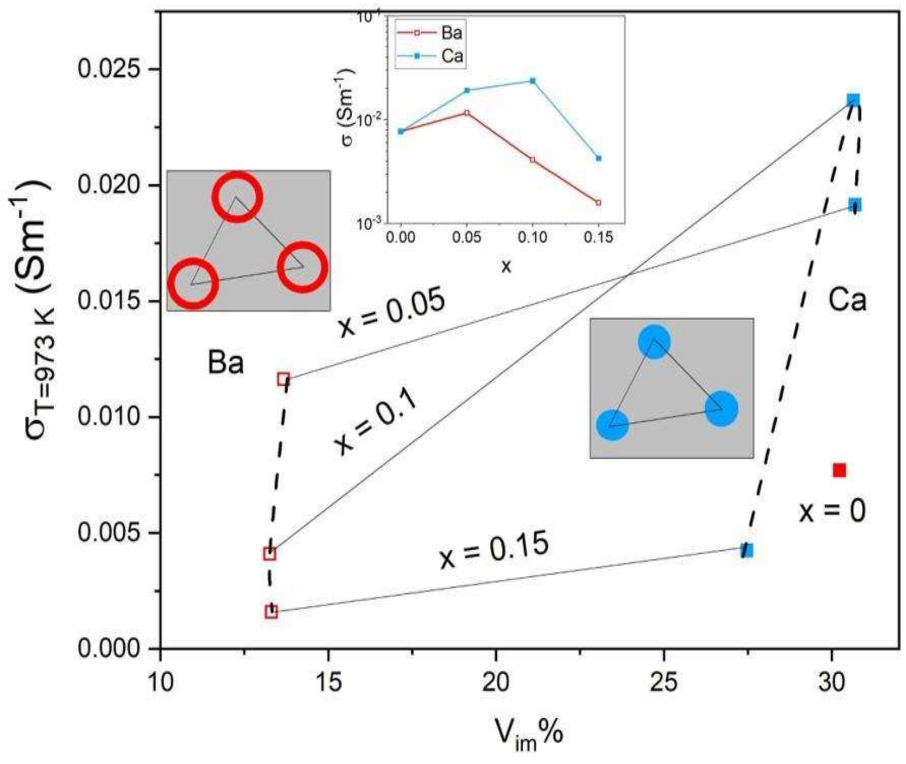

Figure 4.16. Variation of conductivity at 973 K with ion mobility volume for Ca and Ba substituted samples (inset) Variation of conductivity at 973 K with x

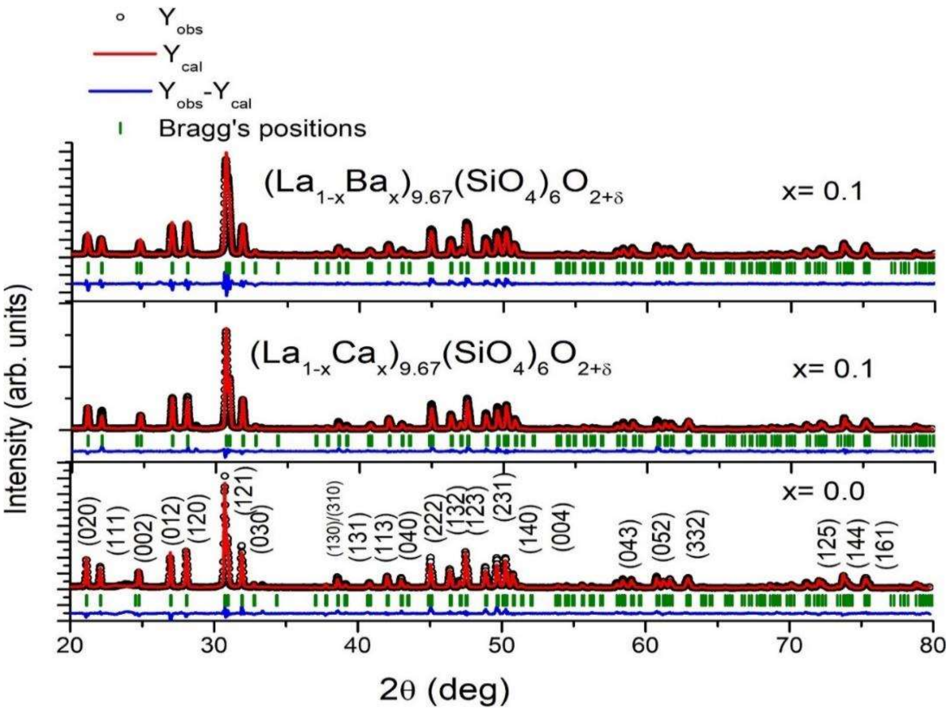

Figure 4.17. Comparative of Rietveld refinement of x = 0.0 and Ca and Ba substituted samples with x = 0.1

Figure 4.17 shows the Rietveld refined X-ray diffractograms of the parent, Ba and Ca substituted samples with x = 0.1. The refinement is done with $P6_3/m$ symmetry using Full Prof Suite package after applying instrumental correction and Pseudo-Voigt peak profile. However, the supplementary shows the detailed refinement and parameters as FIg.4.1-4.4 and Tables 4.1 and 4.2. The goodness of fit ($\chi^2 < 10$) is also mentioned in Fig. 4.3(a) and 4.4(a). We have observed single phase lanthanum silicate in Ba and Ca substituted samples and at x = 0.15, a secondary phase at $2\theta \approx 33^\circ$ corresponding to BaO is observed (JCPDS file No. 01-0746). In comparison to Ba substituted samples, we have observed a secondary phase corresponding to SiO_2 in Ca substituted samples. Further in Ba substituted samples, the peak splitting corresponding to $2\theta \approx 32^\circ$ doesn't completely disappear but reduces with the increase in x (Fig.4.3 right panel). However, on a comparative note, splitting disappears in Ca substituted samples. Further, the lattice parameters and ion mobility volume using bond valence sum calculations have been illustrated in Fig.4.5-4.6 for the Ba and Ca substituted samples.

It can be seen through Fig. 4.18 that on a comparative note, the dense grains with minimal porosity is observed for Ca substituted sample. Further, for Ba substituted sample, x = 0.1, smaller grains with some porosity are observed. However, the grains are hexagonal in shape for Ba and Ca substituted samples. Moreover, at x = 0.0, the polycrystalline microstructure is observed. The morphology changes and grain size alteration with x are shown in Supplementary Fig. 4.7 and Fig. 4.8. Further, to determine the elemental concentration we have used XPS and TGA.

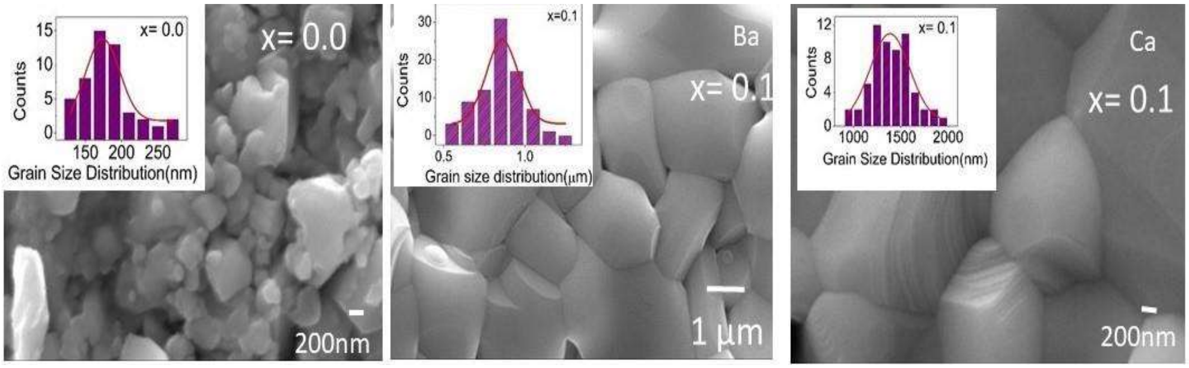

Figure 4.18. Variation of grain size and morphology with x for parent and Ca and Ba substituted samples

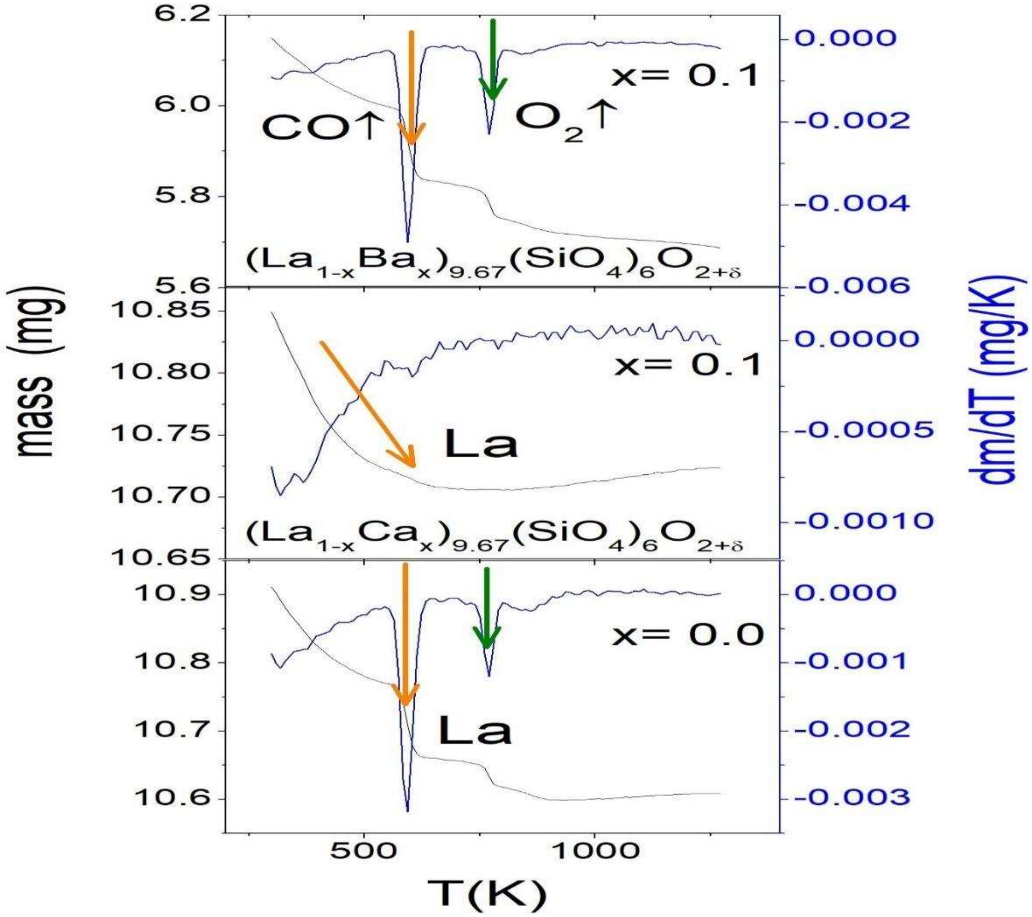

Figure 4.19 TGA for x = 0.0, x= 0.1 Ba and x= 0.1 Ca substituted samples in

$(La_{1-x}A_x)_{9.67-\alpha}(SiO_4)_6O_{2+\delta}$

A gradual mass loss is observed in Thermogravimetric (TGA) curves for all studies samples i.e., $(La_{1-x}A_x)_{9.67-\alpha}(SiO4)_6O_{2+\delta}\ where\ x\ =\ 0.0, 0.05, 0.10\ and\ 0.15$ with A = Ba and Ca (For details see supplementary (Fig. 4.19-4.20)). Here, for a comparative purpose, TGA for x = 0.0, x= 0.1 Ba and x= 0.1 Ca substituted samples are shown in Fig.4.20. In the parent sample, kinks correspond to the weight loss due to La. While with Ba substitution, these kinks correspond to the weight loss due to CO and O_2 as the weight loss observed in both the kinks are nearly 6% and 0.43% correspond to that of CO and O_2. For Ca modified system i.e., $(La_{1-x}Ca_x)_{9.67-\alpha}(SiO_4)_6O_{2+\delta}\ (x\ =\ 0.0, 0.05, 0.10\ and\ 0.15)$, there is a gradual mass loss and weight loss observed in is ~5.8% and matches the weight loss due to La. This suggests the formation of O deficient Ba substituted samples and La deficient parent and Ca substituted samples. The La and O deficiency observed is in accordance with the La content estimated from Rietveld refinement. In order to verify elemental content, XPS spectra has been deconvoluted.

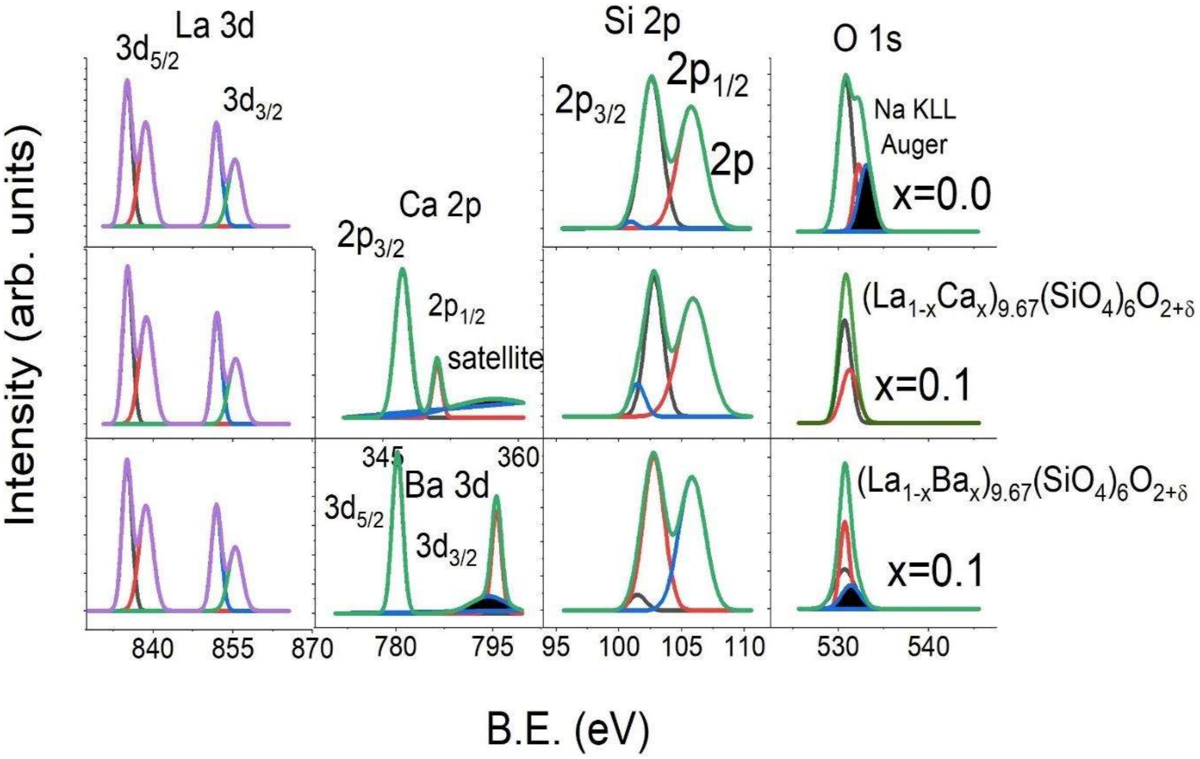

Figure 4.20. Deconvoluted XPS spectra corresponding to La, Ba, Ca, Si and O for x = 0.0, x= 0.1 Ba and x= 0.1 Ca substituted samples in $(La_{1-x}A_x)_{9.67-\alpha}(SiO_4)_6O_{2+\delta}$

The La 3d spectrum shows three chemical states corresponding to La_2O_3, $La(OH)_3$ and La_2CO_3 with well-defined and separated spin components and energies (ΔE, spin orbit splitting) corresponding to 4.6 eV, 3.9 eV and 3.5eV, respectively. In Ca substituted sample, we have observed ΔE ~4.0eV corresponding to the spin orbit splitting corresponding to $La(OH)_3$. In Ba substituted sample, we have observed ΔE ~3.5 eV corresponding to the spin orbit splitting corresponding to La_2CO_3. In Ca2p spectra (< 1eV), chemical shift with the increase in x is observed (Fig.4.11 and variation Ba spectra with x is shown in Fig.4.12). Further, Ca2p has spin orbit components with ΔE ~3.5eV. Here, shake-up satellite is also observed but it cannot be resolved into its components as standard ones. In Ba 3d spectra, Ba loss peak is merged with the 3d3/2 peak affecting the O content (s-d interaction). Si 2p spectrum exhibits ΔE ~0.63 eV i.e., very close spin orbit splitting. Thus, we have observed asymmetric peaks corresponding to Si 2p. Further, the intensity of Si 2p3/2 content is higher in Ca substituted sample than the parent and Ba substituted sample. In O spectra, O 1s peak at ~529 eV is linked to the metal and O bond (La-O, Si- O and Ca-O) while, 2nd peak of O belongs to metal-OH bond. Oxygen vacancy concentration is linked to the ratio of peak area corresponding to the M-O and M-OH bond. The intensity of M-OH peak is higher in Ba substituted sample rather than the parent and Ca substituted sample, Further, Na KLL Auger peak is observed in x = 0.0 and in Ca substituted sample, Auger peak diminishes. But in Ba substituted sample, Auger peak do not diminish. The occurrence of satellite peak in Ca 2p spectra and disappearance of Auger peak in O 1s spectra is due to metal ligand interaction i.e. interaction of s orbital of Ca and p-orbital of O (s-p interaction). In addition, the formation of $La(OH)_3$ in Ca substituted sample suggests the formation of La vacancies and the samples are found to be La and Si deficient from the occupancies observed from the Rietveld refinement. On a comparative note, Ba substituted samples are more oxygen deficient due to the formation of La_2CO_3. Further, elemental content has been estimated from XPS.

It is observed in Fig. 4.21 (a) that grain size (obtained from grain size histograms) is increasing with x with an exception at x = 0.15 in Ca substituted samples and grain size increases with x in Ba substituted samples. In Ca substituted samples, the trend of grain size is like the trend in La content (Fig.4.21(b)). Further, Si and O are behaving opposite to each other i.e., with the increase in x Si content increases (Fig.4.21(c)) and O content decreases (Fig. 4.21(d)). In Ba substituted samples, the trend of grain size is like the trend in O content. Here, (La+Ba) and Si content have no definite trend with x. Thus, this result is in accordance with the La deficiency for Ca substituted and O deficiency for Ba substituted samples. This can be understood as follows. The formation of $La(OH)_3$ suggests the formation of La vacancies and the samples are found to be La and Si deficient from the occupancies observed from the Rietveld refinement in Ca substituted sample with the higher ion mobility volume. The formation of $LaCO_3$ suggests the formation of O vacancies and the samples are found to be O deficient from the occupancies observed from the Rietveld refinement in Ba substituted sample with the lower ion mobility volume.

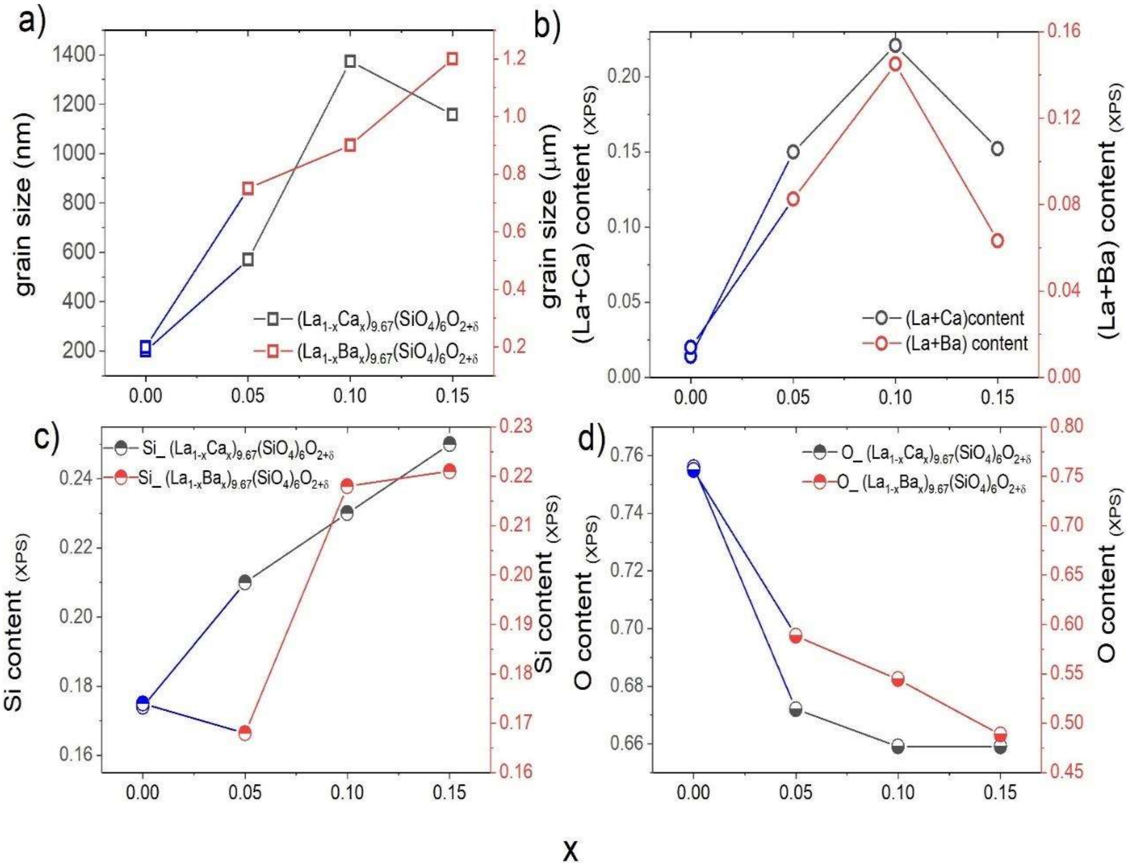

Figure 4.21. (a) Grain size obtained from SEM micrographs (grain histograms) for Ca and Ba substituted samples (b) La+ Ba content extracted from XPS, La+Ca content extracted from XPS (c) Si content from XPS (d) O content from XPS (lines are a guide to eye)

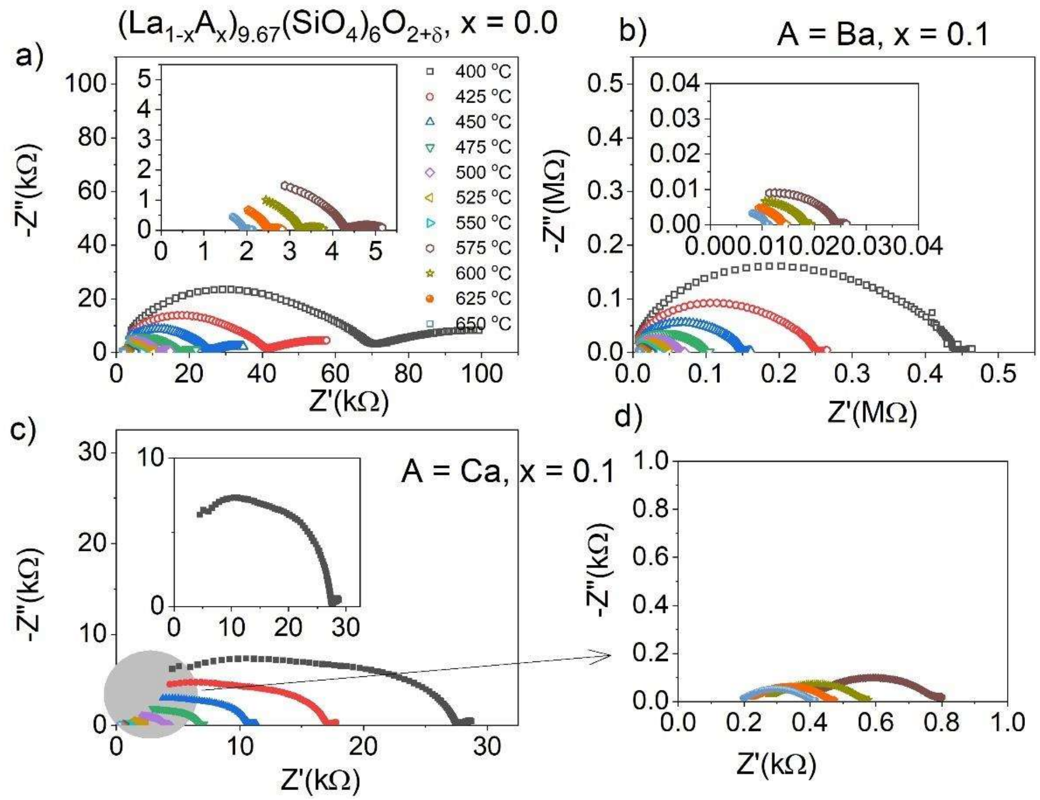

Figure 4.22: Nyquist plots taken over a wide frequency range (20 Hz to 1 MHz) at different temperatures (400 °C to 650 °C) for $(La_{1-x}A_x)_{9.67}(SiO_4)_6O_{2+\delta}$ system (a) x = 0.0 (b) x = 0.1 with A = Ba, and (c) x = 0.1 with A = Ca, (d) zoomed portion of Nyquist plot at high temperatures (575 °C to 650 °C)

Figure 4.22 shows plot of Z' vs Z'' (Nyquist plots) taken over a wide frequency range (20 Hz to 1 MHz) at different temperatures (400 °C to 650 °C) for $(La_{1-x}A_x)_{9.67}(SiO_4)_6O_{2+\delta}$ system (a) x = 0.0 (b) x = 0.1 with A = Ba, and (c) x = 0.1 with A = Ca, (d) zoomed portion of Nyquist plot at high temperatures (575 °C to 650 °C). The depressed semicircles with off-centring on x-axis indicating non- Debye behaviour are observed. However, two semicircles in the Nyquist plots are observed for parent and Ba substituted sample indicating the presence of grain and grain boundary effects. Whereas, in Ca substituted samples, three semicircles in the Nyquist plots are observed for Ca substituted sample exhibiting grain, grain-boundary and electrode effects. The grain, grain-boundary and electrode resistances at different temperatures are estimated from the Nyquist or Cole–Cole plots. Figure 4.23 depicts the Arrhenius plots for the grain, grain-boundary and electrode resistances. Here, it is observed again the deviation of fitted lines from the data points. Thus, activation energies are estimated in the two regimes for the parent, Ba and Ca substituted samples. The two slopes are observed in Arrhenius plots of grain, grain-boundary and electrode resistance. This confirms our earlier observation of two slopes observed in the dc conductivity plots (Fig. 4.7). Now the slopes can be attributed to the extrinsic contribution at the interface due to the varying charge concentrations at bulk and grain-boundary interfaces (can also be seen through EDX). Moreover, it is also observed that grain, grain boundary and electrode resistances are observed to decrease with increase in temperature manifesting NTCR (negative temperature coefficient of resistance) behavior.

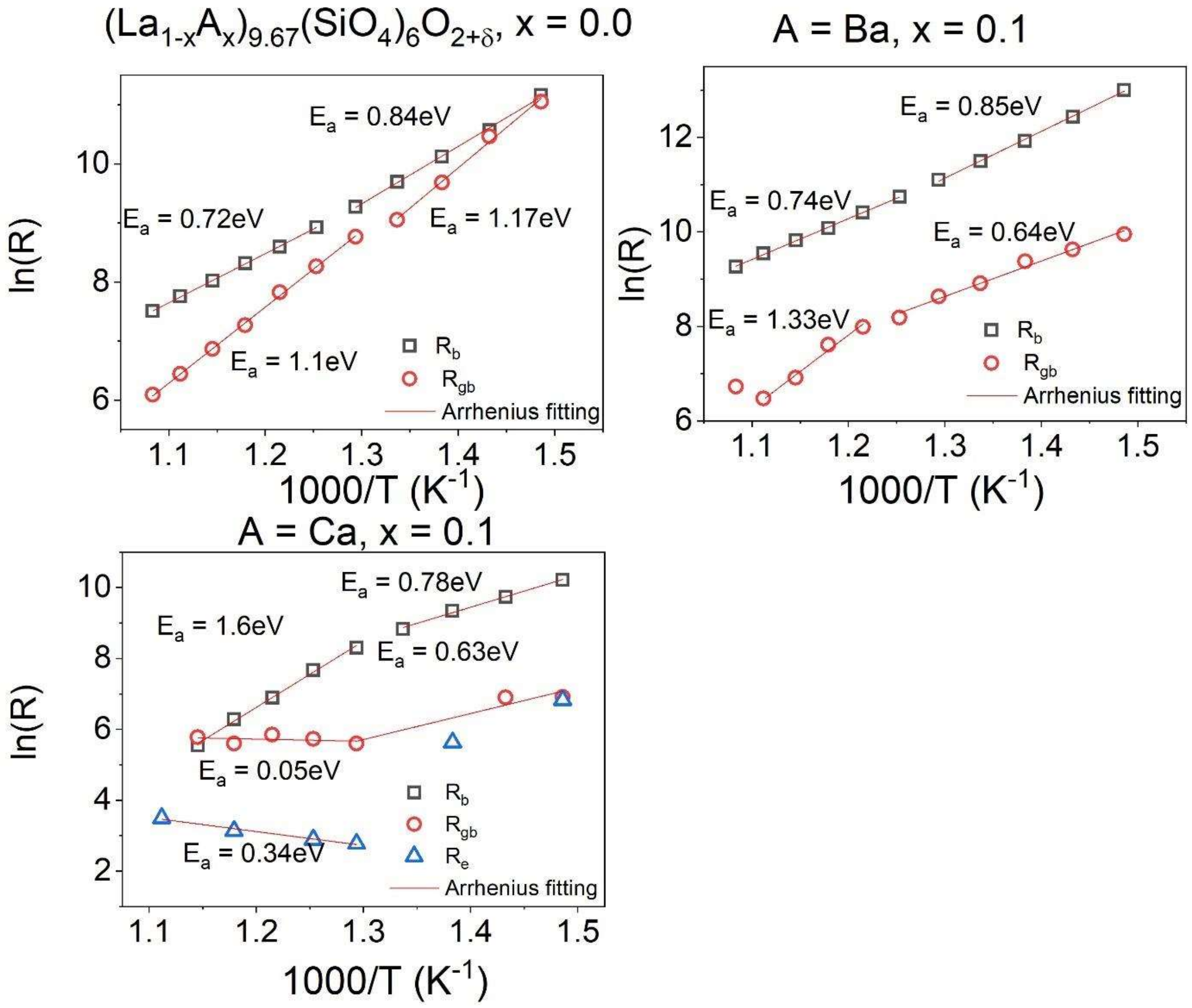

Figure 4.23: Arrhenius plots for the grain, grain-boundary and electrode resistances. Here, it is observed again the deviation of fitted lines from the data points. Thus, activation energies are estimated in the two regimes for the $(La_{1-x}A_x)_{9.67}(SiO_4)_6O_{2+\delta}$ system (a) x = 0.0 (b) x = 0.1 with A = Ba, and (c) x = 0.1 with A = Ca.

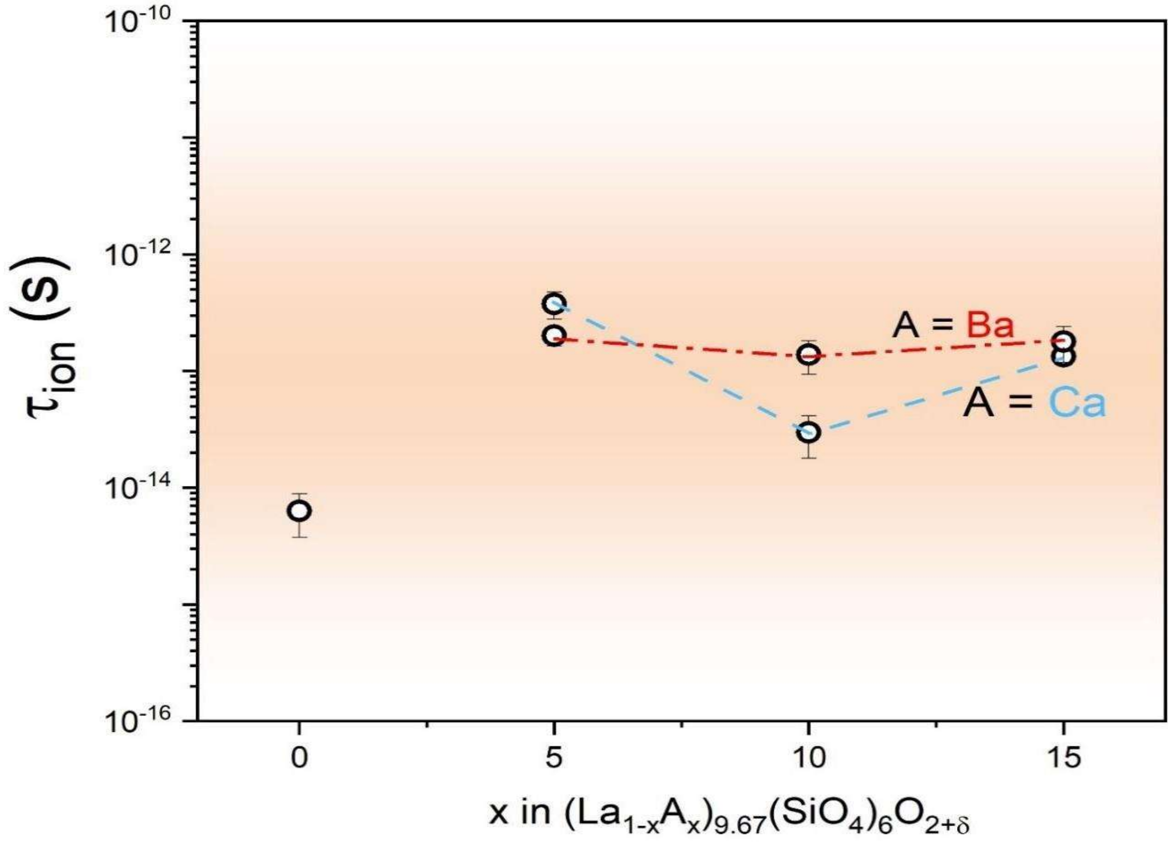

Figure 4.24 Value of mean free ion lifetime with x

The mean free ion lifetime estimated by the probability of transition rate from occupied site to unoccupied site with x is shown in Fig. 4.24. The data is well fitted with the model showing $\chi^2 > 0.99$ up to 800 K.

$$\frac{1}{\tau} = \frac{1}{\tau_0} \exp\left(-\frac{E_0}{k_B T}\right) \tag{4.2}$$

The ionic conductivity equation is,

$$\sigma = \frac{1}{3}\left(\frac{(Ze^2)}{k_B T}\right) n_i a_0^2 \omega_0 \exp\left(-\frac{E_0}{k_B T}\right) \tag{4.3}$$

Using equation 1 and 2,

$$\frac{\sigma}{\omega} = \frac{1}{3}\left(\frac{(Ze^2)}{k_B T}\right) n_i a_0^2 = \alpha n_i \qquad (4.4)$$

where n_i is number density of ionic species, a_0 is the hopping length. We can see that for x = 0.0, the mean free life time is 10^{-14} s (intramolecular vibration modes) while for the Ca and Ba modified compositions, the mean free ion life time is between 10^{-12} s (intermolecular vibration modes) and 10^{-14} s (intramolecular vibration modes) and 10^{-17} s. It is accounting for the vacancy diffusion mechanism with the formation of polarons due to oxygen deficiency.

4.5 DISCUSSION AND CONCLUDING REMARK

Here, with the ionic radii variation, ion mobility volume has risen to nearly 3 times in Ca substituted sample rather than Ba substituted sample. Moreover, La deficient Ca substituted samples and O deficient Ba substituted samples are obtained. Further, XPS, TGA and Rietveld refinement confirm the formation of La and O deficient Ca and Ba substituted samples, respectively. Moreover, s-p interaction is playing a critical role in the conductivity mechanism of Ca substituted sample. Whereas, loss is occurring due to metal ligand interaction (s-d interaction) in Ba substituted sample. The conductivity, due to connected grain growth increased for x = 0.1 in Ca substituted sample can be attributed to the different local disorder by La vacancy, higher ion mobility volume and s-p interaction. On a comparative note, conductivity reduces in Ba substituted sample due to the decrease in ion mobility volume, creation of O vacancies and s-d interaction.

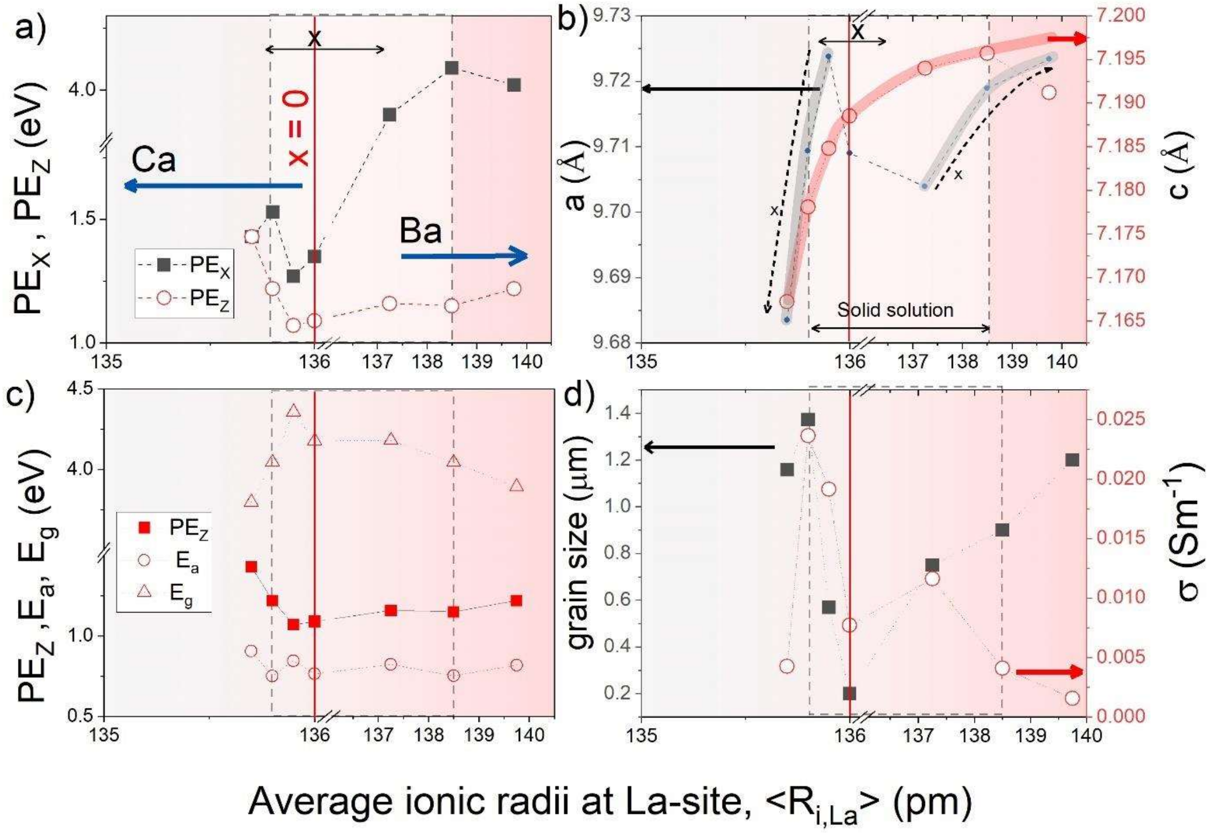

Figure 4.25: Variation of (a) percolation energy along the x-axis (PE_X) and z-axis (PE_Z), (b) lattice parameters a and c, (c) PE_Z, activation energy (E_a.) and band gap energy (E_g), and (d) grain size and conductivity with average ionic radii at La site $<R_{i,\, La}>$.

Figure 4.25 (a) shows the variation of percolation energy along the x-axis (PE_X) and z-axis (PE_Z) with $<R_{i,\, La}>$. The vertical solid red line is reference line for x = 0. It can be observed that for lower $<R_{i,\, La}>$ i.e., Ca substitution, percolation energy is < 1.5 eV in both the directions. Additionally, both PE_X and PE_Z are particular decreasing with x (at least with in solubility limits i.e., $x \leq 0.1$ dotted lines). However, in case of materials with greater $<R_{i,\, La}>$ i.e., with Ba substitution, PE_Z shows very small (almost constant) rise with the increase in x. But the interesting feature is observed for PE_X, it is increasing sharply to ~ 4 eV with x. The percolation energy is interrelated to both the structural parameters as well as ion dynamics of materials. Mathematically, it is expressed as $PE = E_a - \beta I(a_o)$, where $I(a_o)$ is energy overlap integral which function of a_o (separation between two donors), β is percolation constant [145]. Recently overlapping large polaron tunnelling is observed for these compounds[146]. Thus, energy overlap integral and hence lattice parameter should be instrumental for understanding the observation of high value of conduction in substituted compounds (in spite of significant lower volume for ion mobility). Figure 4.25 (b) shows the variation of lattice parameters 'a' and 'c' with $<R_{i,\ La}>$. A monotonic relation is observed in between lattice parameter c and $<R_{i,\ La}>$. While variation of lattice parameter 'a' is subject to substituents' content but not monotonous with $<R_{i,\ La}>$. This suggests the lattice deformation is significant in a-b plane (concentric hexagons, Fig.4.15(b)) while c-axis (O4 channel, Fig. 4.15(c)) remains almost unaltered. Further, it is also observed in Fig. 4.25(c) that variation of activation energy, E_a, is almost similar to the variation of PE_Z. However, the band gap energy (Fig. 4.25(c), estimated from Tauc plots shown in supplementary, Fig.4.24) has the opposite trend to that of activation energy and percolation energy along z-axis. This suggests that the conduction should be prominent along O4 channel. It is well known that larger band gap reduces the electronic conductivity and promotes the ionic conductivity. Thus, for the Ca substituted sample higher band gap is accounted for higher ionic conductivity instead of Ba substituted samples. This observation is in accordance with the s-p interaction and s-d interaction observed in case of Ca and Ba substituted samples, respectively. Furthermore, grain connectivity also plays a pivotal role in ionic conduction. Thus, the variation of grain size and conductivity with $<R_{i,\ La}>$ are shown in Fig. 4.25(d). Here, it is observed that within the solid solubility limit, conductivity has the same trend as grain size except for Ba substitution with x = 0.10 and x = 0.15. Also, the variation of grain size is nearly similar to PE_Z within solubility limit. Hence, it can be summed up as percolation energy, activation energy, band gap, lattice parameter and grain size are controlled via average ionic radii at La site in case of $(La_{1-x}A_x)_{10-\alpha}(SiO_4)_6O_{2+\delta}$ i.e., $PE_z \propto c \propto grainsize \propto E_a \propto (1/E_g) \propto \sigma \propto < R_{i,La} >$.